The astroglial protein S100β regulates axon initial segment plasticity

Rafael Sanz-Gálvez[1,2]†, Yanis Inglebert[1,2]†, Arlette Kolta[1,2,3]

[1]Department of Neurosciences, Université de Montréal, Montréal, Canada

[2]Centre Interdisciplinaire de recherche sur le cerveau et l'apprentissage (CIRCA), Montréal, Québec, Canada

[3]Faculté de Médecine Dentaire, Université de Montréal, Montréal, Québec, Canada.

†These authors contributed equally to this work and share first authorship

Corresponding authors: arlette.kolta@umontreal.ca

Keywords: Astrocytes, Intrinsic Excitability, LTP-IE, Visual Cortex, S100β, Axon Initial Segment

34 pages, 82 references, 5 figures, 4 Supplementary figures

ABSTRACT

One key regulator of neuronal excitability is the axon initial segment (AIS), a highly specialized axonal region, enriched in ion channels, where action potentials are initiated. The AIS can undergo significant morphological changes to fine-tune neuronal excitability in response to external perturbations. Long considered solely a homeostatic mechanism operating over long timescales (hours to days) to adjust excitability, we show here that this phenomenon can also occur rapidly, within minutes, following a brief period of high activity in layer 5 pyramidal neurons of the visual cortex. Because astrocytes have been known to regulate neuronal excitability, we explored the effects of gliotransmitters on this process and identified the calcium-binding protein S100β from astrocytes to be required for the rapid reorganization of the AIS.

INTRODUCTION

The plasticity of the input-output function is regulated by diverse plasticity rules to adapt neuron' excitability in response to external or internal perturbations. One powerful regulator is the axon initial segment (AIS), a specialized subcellular region of the proximal axon where action potentials are shaped and initiated (Debanne et al., 2011). Structural plasticity of the AIS can influence neuronal output as demonstrated by changes in AIS length in response to external perturbation to maintain appropriate neuronal excitability (Yamada and Kuba, 2016; Fréal et al., 2023). The length of the AIS is a reliable indicator of neuronal excitability, where increased length enhances excitability and decreased length lowers it. Plasticity of the AIS is highly used in different sensory processing brain regions to fine-tune neuronal excitability or during development to maintain stable network excitability (Kuba et al., 2006; Schlüter et al., 2017). For instance, in the visual cortex, the AIS is developmentally regulated by visual experience during critical period (Gutzmann et al., 2014; Höfflin et al., 2017). Historically, AIS plasticity has been considered a homeostatic mechanism operating over long timescales (days to weeks), allowing neurons to maintain their firing set point in response to network perturbations. This view largely stems from studies conducted in neuronal cultures following chronic network manipulations (Grubb and Burrone, 2010). This perspective has evolved

over time, with plasticity being described at progressively shorter timescales, from hours to minutes (Grubb et al., 2011; Evans et al., 2015). The latest findings, using newly developed genetic tools (Thome et al., 2025) that label the scaffolding protein Ankyrin G (AnkG), a specific marker of the AIS (Leterrier, 2018) reveal that AIS reorganization can occur within minutes following long-term depression in the hippocampus (Fréal et al., 2023). This is the first evidence showing that the synergistic excitability changes observed following synaptic plasticity could be accompanied by AIS plasticity (Campanac and Debanne, 2007, 2008). However, synaptic plasticity is not the sole mechanism of memory storage; intrinsic excitability plasticity can also occur in response to non-homeostatic stimulation and could be associated as well with rapid AIS plasticity, a possibility that, until now, has never been tested. Here, we provide initial evidence of a close relationship between intrinsic excitability changes and AIS plasticity. In Layer 5 cortical pyramidal neurons (L5PNs), repetitive bursts high-frequency firing induce long-term potentiation of intrinsic excitability (LTP-IE) a fundamental mechanism to refine visual circuit (Cudmore and Turrigiano, 2004; Nataraj et al., 2010; Duménieu et al., 2025). In cortical circuit, LTP-IE is dependent on extracellular calcium influx and modulation of ion channels (Cudmore and Turrigiano, 2004). Among the various external factors that could influence LTP-IE, astrocytes have long been overlooked despite increasing evidence of their role as powerful modulators of input-output functions and sensory processing (Sanz-Gálvez et al., 2024). Recent findings show that astrocytes directly interact with the axon or the AIS to modulate excitability through the release of gliotransmitters (Debanne and Rama, 2011; Lezmy et al., 2021). Moreover, in murine models of Alzheimer's disease, AIS integrity and length deteriorate due to transcriptomic and proteomic alterations in astrocytes (Benitez et al., 2024). One relatively understudied gliotransmitter, S100β, is particularly intriguing as it functions both as a calcium (Ca^{2+})-binding protein to regulate the concentration of extracellular calcium and a modulator of various voltage-gated ion channels (Hermann et al., 2012; Bancroft et al., 2022). Extracellularly, it primarily binds to membrane receptors such as the multi-ligand Receptor for Advanced Glycation End Products (RAGE), triggering intracellular signaling cascades that, depending on its concentration, may lead to physiological or pathological outcomes (Donato

et al., 2009). We have previously shown that S100β and stimulation of astrocytes (presumably through release of S100β) elicit spiking in L5PNs from the visual cortex and trigeminal primary afferent axons or promote rhythmic activity in trigeminal sensori-motor circuit through the enhanced activation of voltage-gated sodium (NaV) 1.6 channels (Morquette et al., 2015; Ryczko et al., 2021; Gaudel et al., 2025). Interestingly, NaV 1.6 is one of the main isoforms of NaV channels expressed at the AIS in excitatory neurons which distribution is reorganized during plasticity (Fréal et al., 2023). Here, we first test whether LTP-IE is associated with rapid AIS plasticity in L5PNs of the visual cortex and then examine if astrocytes regulate this process through the release of the gliotransmitter S100β.

RESULTS

Long-lasting potentiation of intrinsic excitability (LTP-IE) is associated with rapid AIS plasticity

Layer 5 pyramidal neurons (L5PNs) were recorded in acute slices from the primary visual cortex (V1) obtained from Vglut2-AnkG-GFP young mice (P14–P30) (see Methods and **Fig. 1A**), and their intrinsic excitability was monitored by a 500-ms constant direct current pulse every 10 seconds for 5 min after which repetitive current injection (500-ms depolarizing pulses, 60 times at 4-second interval, **Fig. 1B bottom)** was used to induce long-lasting potentiation of intrinsic excitability (LTP-IE). All experiments were conducted in the presence of glutamatergic and GABAergic receptors blockers to prevent interferences from synaptically released fast excitatory and inhibitory neurotransmitters. As previously described (Cudmore and Turrigiano, 2004), this protocol induced a robust and long-lasting increase in intrinsic excitability (151% ± 12, n=6, **Fig. 1B**), which was monitored every 10 seconds for 30 minutes after induction. After confirming our immunohistochemical results showing that the GFP signal colocalized with the master AIS protein, AnkG (**Fig. 1A top**), we proceeded to monitor AIS remodeling in real-time before and after the induction protocol in the recorded neuron filled with Alexa Fluor 647 (**Fig. 1A bottom**). Fluorescence images of AnkG-GFP taken 30 minutes after induction revealed a rapid and significant elongation in the distal part of the AIS, as confirmed by fluorescence intensity measurements (mean AIS length: 29.68 ± 1.25 µm before induction and 33.29 ± 1.35 µm after induction, n=6, t-test, $P<0.001$; **Fig. 1C**). To avoid rapid deterioration due to phototoxicity, imaging of the AIS was

87 minimized, but in a separate set of experiments (n=5), images were captured every 5 minutes,
88 revealing that in some cells, the increase began as early as 10–15 minutes after induction
89 **(Fig. S1)**. In the absence of the induction protocol, no LTP-IE (102% ± 2, n=5, **Fig. 1B**) or AIS
90 remodeling was observed (mean AIS length: 34.31 ± 0.95 μm before and 34.21 ± 0.92 μm
91 after, n=5, t-test, P>0.05; **Fig. 1F**). To determine changes in neuronal excitability, the number
92 of APs for each increase in injected current was counted, establishing input-output curves
93 before and after the induction protocol. Additionally, rheobase, an important parameter of
94 neuronal excitability, was measured. In neurons subjected to the brief repetitive firing period,
95 a significant increase in intrinsic excitability was observed across other supra-threshold
96 current amplitudes (from 30 pA to 100 pA, t-test, P<0.01; P<0.05; **Fig. 1D**), whereas no
97 significant changes were observed in control neurons (all steps; t-test, P>0.05; **Fig. 1G**).
98 Moreover, in neurons subjected to the induction protocol, but not in control neurons (**Fig.**
99 **1H**), a significant decrease in rheobase was observed (30 ± 12 pA before vs. 21 ± 9 pA after
100 induction, n=6, t-test, P<0.01; **Fig. 1E**). Together, these data demonstrate that a period of
101 high-frequency activation as brief as 4 min suffice to induce remodeling of the AIS and LTP-
102 IE in L5PNs.

103 **LTP-IE and AIS plasticity involves peri-AIS astrocyte signaling**

104 Astrocytes are involved in various forms of synaptic plasticity (Yang et al., 2003; Andersson
105 et al., 2007; Falcón-Moya et al., 2020; Sanz-Gálvez et al., 2024); however, their potential
106 contribution to intrinsic plasticity has not been assessed. Therefore, we examined whether
107 peri-AIS astrocytes (astrocytes near the AIS) are necessary for LTP-IE and the consequent
108 structural remodeling of the AIS in L5PN neurons. To address this, we preincubated acute
109 brain slices for 5 minutes RT with Sulforhodamine (SR101, 1 μM), a widely used astrocyte
110 marker in different brain regions (**Fig. 2A**) (Watanabe et al., 2023). Next, a single astrocyte
111 was loaded with 20 mM of the Ca^{2+} chelator BAPTA via a patch pipette to inhibit Ca^{2+}-
112 dependent vesicular release and gliotransmitter signaling (Araque et al., 1998) and a nearby
113 L5PN (distance between the AIS of the recorded neuron and the patched astrocyte; 37.02 ±
114 8.74 μm, **Fig. 2B**) was targeted for whole-cell recording after allowing time (15 min) for BAPTA
115 to diffuse in the astrocytic syncitium. Astrocytic inactivation with BAPTA prevented the

116 induction of LTP-IE (103% ± 4, n=5; **Fig. 2B**) and the associated AIS lengthening (mean AIS
117 length: 33.4 ± 0.95 µm before induction vs. 32.61 ± 0.94 µm after induction, n=5, t-test,
118 P>0.05; **Fig. 2C**). No significant changes were observed in input-output curves or rheobase
119 values before and after induction (**Fig. 2D,E**). Taken together, these results clearly indicate
120 that peri-AIS astrocytes are required for the induction of this form of intrinsic excitability
121 plasticity and AIS remodeling.

122 **LTP-IE and AIS plasticity depend on the astrocytic protein S100β**

123 In the visual cortex, LTP-IE, as other types of synaptic plasticity, depends on extracellular Ca^{2+}
124 (Inglebert et al., 2020), since it is abolished in 0mM Ca^{2+} medium (Cudmore and Turrigiano,
125 2004). Our previous studies demonstrated that astrocytes could tightly regulate extracellular
126 Ca^{2+} levels through the release of S100β (Morquette et al., 2015) and that optogenetic
127 activation of layer 5 astrocytes in the visual cortex decreases extracellular Ca^{2+} via S100β
128 release (Ryczko et al., 2021). Based on these findings, we investigated whether this Ca^{2+}-
129 binding astrocytic protein could locally modulate LTP-IE and AIS structural remodeling. To
130 this end, we locally administered an anti-S100β antibody in the vicinity of the AIS for 5
131 minutes prior to induction to prevent the endogenous protein from exerting its effects and
132 from binding Ca^{2+} (Morquette et al., 2015). Applications of the same antibody, but
133 denaturated by preheating to 100 degrees Celsius for 20 minutes, served as controls. The
134 S100β antibody effectively blocked LTP-IE, whereas the denatured antibody did not preclude
135 its induction (S100β antibody: 106% ± 17, n=5 vs. S100β antibody denatured: 180% ± 9, n=6,
136 (MW) U test, P<0.05; **Fig. 3A**). Confocal imaging further revealed that the S100β antibody
137 prevented AIS elongation (mean AIS length: 34.76 ± 0.41 µm before induction and 34.48 ±
138 0.48 µm after induction, n=5, t-test, P>0.05; **Fig. 3B**). Conversely, with the denatured
139 antibody, significant AIS elongation was observed (mean AIS length: 32.45 ± 1.67 µm before
140 induction and 34.63 ± 1.62 µm after induction, n=6, t-test, P<0.001; **Fig. 3E**) similar to what
141 is observed in control condition (**Fig 1C**). The S100β antibody application was found to cause
142 a small decrease of excitability as measured in the input-output curves, but this change was
143 not statistically significant (all steps; t-test, P>0.05; **Fig. 3C**). This effect is likely attributable
144 to an increase in extracellular Ca^{2+} levels induced by S100β blockade, which is consistent

145 with prior findings indicating that elevated extracellular Ca^{2+} levels suppress neuronal
146 excitability (Forsberg et al., 2019, 2025). In contrast, the denatured antibody application is
147 associated with an upward shift of the input-output curve (pA40, pA60-pA100, t-test, $P<0.05$;
148 **Fig. 3F**). No significant changes were observed in rheobase under any condition (**Fig. 3D,G**).
149 Collectively, these data underscore the necessity of the Ca^{2+}-binding astrocytic protein
150 S100β for the induction of LTP-IE and AIS morphological modifications in LPN5s.

151 **Optogenetic activation of peri-AIS astrocytes induces LTP-IE and AIS plasticity through S100β**
152 **release**

153 Having established that astrocytes and S100β are critically involved in mediating LTP-IE and
154 AIS remodeling, we next aimed to determine whether selective activation of peri-AIS
155 astrocytes alone could suffice to induce LTP-IE. To address this, neonatal VGlut2-AnkG-GFP
156 mice (P0) were bilaterally injected intracerebrally with an adeno-associated virus (AAV)
157 expressing Channelrhodopsin-2 (ChR2) fused to the mCherry reporter and targeted to
158 astrocytes using the GFAP promoter (**Fig. 4A left**). To verify that viral transfection was
159 specifically restricted to astrocytes, immunohistochemistry was performed on V1 sections
160 using an antibody against S100β. Immunostaining revealed that viral expression was targeted
161 to astrocytes, as evidenced by the colocalization of mCherry/ChR2-GFAP with S100β (**Fig.**
162 **4A right**). Next, in acute brain slices, patch-clamp recordings demonstrated that transfected
163 astrocytes responded to light pulses (using a combination of 440 nm and 488 nm lasers from
164 a confocal microscope) by evoking membrane depolarizations (**Fig. S2**). This response was
165 verified in representative experiments (**see Methods**). Additionally, we confirmed that viral
166 transfection did not affect the real-time visualization of AIS morphology (**Fig. 4B bottom left**).

167 Subsequently, excitability of L5PNs was assessed as above, but the induction protocol was
168 substituted by photostimulation of astrocytes (short light pulses of 2 seconds on, followed
169 by 2 seconds off, repeated 60 times; **Fig. S2**) which was as efficient for induction of LTP-IE
170 (**Fig. 4B**). Importantly, local administration of the S100β antibody for 5 minutes prior to
171 optogenetic stimulation of peri-AIS astrocytes abolished LTP-IE (opto Astro: 160% ± 10, n=6
172 vs. S100β antibody + opto Astro: 101% ± 3, n=6; (MW) U test, $P<0.01$; **Fig. 4B**). Confocal
173 imaging revealed a significant elongation of the AIS length 30 minutes after optogenetic

174 stimulation of peri-AIS astrocytes (mean AIS length: 31.96 ± 2.05 μm pre-stimulation vs.
175 35.25 ± 2.20 μm post-stimulation, n=6, t-test, P<0.01; **Fig. 4C**), which was prevented when
176 the S100β antibody was applied locally (mean AIS length: 33.14 ± 1.98 μm pre-stimulation
177 vs. 32.85 ± 2.15 μm post-stimulation, n=6, t-test, P>0.05; **Fig. 4D**). Input-output curves
178 showed that responses to suprathreshold current amplitudes significantly increased after
179 optogenetic stimulation of peri-AIS astrocytes (pA30-pA80, t-test, P<0.01; P<0.05; **Fig. 4E**),
180 whereas no changes were observed when the S100β antibody was applied prior to optical
181 stimulation (all steps; t-test, P>0.05; **Fig. 4F**). Changes in rheobase values were observed in
182 recorded neurons after optogenetic activation of peri-AIS astrocytes (33 ± 15 pA before vs.
183 25 ± 10 pA after stimulation, n=6, t-test, P<0.05; **Fig. 4E**), whereas no significant changes
184 were detected following prior application of the S100β antibody before activation (**Fig. 4F**). It
185 might be expected that S100β is not the only gliotransmitter released by astrocytes to
186 regulate this form of LTP-IE and rapid AIS plasticity. Given that ATP/adenosine released by
187 astrocytes can alter AIS excitability (Lezmy et al., 2021), we decided to test the local
188 administration of Suramin (100 μM) (a purinergic antagonist) for 5 minutes before
189 optogenetic stimulation of astrocytes. However, our results showed that the administration
190 of Suramin did not abolish either LTP-IE or the morphological changes in the AIS (**Fig. S3**).
191 These findings demonstrate that selective activation of peri-AIS astrocytes is sufficient to
192 induce LTP-IE and AIS remodeling, highlighting the crucial involvement of astrocyte-derived
193 S100β in regulating neuronal excitability and axonal plasticity.

194 **The astrocytic protein S100β rescues LTP-IE and rapid AIS plasticity**

195 To further confirm the key role of S100β in LTP-IE and rapid AIS remodeling observed in V1
196 L5PNs, we repeated the previous experiment of astrocytic network inhibition but with local
197 application of S100β (129 μM) for 5 minutes prior to the induction protocol. This approach
198 allowed us to fully saturate the local environment without inducing spiking during the
199 protocol itself, which could otherwise alter the results. Consistent with our previous findings,
200 application of S100β to the proximal axon, while peri-AIS astrocytes were inactivated, was
201 sufficient to rescue LTP-IE (157% ± 12, n=6 vs 102% ± 6, n=5, (MW) U test, P<0.01, **Fig. 5A**).
202 Confocal imaging also revealed rescue of AIS remodeling with S100β application (mean AIS

203 length: 33.45 ± 1.78 µm before induction and 36.57 ± 2.10 µm after induction, n=6, t-test,
204 P<0.01; **Fig. 5B**). Input-output curves showed that responses to suprathreshold current
205 amplitudes significantly increased after application of S100β (pA40-pA100, t-test, P<0.05;
206 **Fig. 5C**). Additionally, significant differences were observed in rheobase values (45 ± 16 pA
207 before vs. 31 ± 14 pA after induction, n=6, t-test, P<0.05; **Fig. 5D**). To insure that the effects
208 of the locally applied S100β resulted from its Ca^{2+} chelating action, we confirmed these
209 findings with the local extracellular application of BAPTA (5 mM) which exerts similar effects
210 on Ca^{2+} (**Fig. S4**). Together, these results further support the role of S100β as a key regulator
211 of LTP-IE and rapid AIS remodeling.

212 **DISCUSSION**

213 Previous studies have shown that the AIS is a highly dynamic structure that contributes to
214 the fine regulation of neuronal output (Grubb and Burrone, 2010; Evans et al., 2013).
215 However, until now, plastic changes in the AIS have been limited to static post-hoc snapshots
216 in large, differentially treated populations, preventing the detection of small-scale changes
217 that may be obscured due to intercellular heterogeneity. Here, we have leveraged a new
218 AnkG-GFP mouse model (Thome et al., 2025) to monitor the AIS in real time at the single-cell
219 level. We found that in the visual cortex, the long-lasting increase of intrinsic excitability (LTP-
220 IE) produced by a brief period of high frequency activity as previously described by Cudmore
221 and Turrigiano (2004) is associated with rapid structural plasticity of the AIS, predominantly
222 characterized by a distal elongation of its length (**Fig. 1**). This observation aligns with previous
223 studies (Kuba et al., 2015; Jamann et al., 2021) showing that AIS elongation is linked to
224 increased intrinsic excitability and a lower action potential (AP) threshold, highlighting a
225 coordinated interplay between functional and structural plasticity of the AIS. Astrocytes have
226 long been recognized as regulators of synaptic transmission, plasticity, and excitability
227 through gliotransmitter release and local ion homeostasis. However, to our knowledge, their
228 potential involvement in the plasticity of intrinsic excitability, including AIS morphological
229 changes, has not yet been explored. We have demonstrated that peri-AIS astrocytes
230 (proximal or adjacent to the AIS) can regulate the structural and functional plasticity of the

231 AIS following brief periods of intrinsic spiking activity. This regulation depends on the release
232 of the astrocytic calcium-binding protein S100β.

233 **LTP-IE is associated with increases AIS**

234 Our results demonstrate that LTP-IE in L5PNs of the visual cortex is associated with a rapid
235 increase in AIS length. This finding is significant, as it highlights the AIS's ability to very rapidly
236 (within minutes) adjust its length to regulate neuronal excitability, while it was believed to
237 occur only on longer timescale (hours to days) acting mostly as a homeostatic mechanism.
238 These results demonstrate that AIS morphology plasticity is also a mechanism allowing a
239 neuron to adapt rapidly its excitability in addition to others such as regulation of ion channels
240 to modulate spike thresholds or EPSP amplification (Debanne and Russier, 2019). LTP-IE in
241 non-homeostatic form has been described in other brain regions including the hippocampus
242 and the brainstem (Nelson et al., 2003; Sourdet et al., 2003) and it would be interesting to
243 know if it is accompanied by changes in AIS morphology as well. The mechanisms described
244 for LTP-IE so far seem to vary from a region to another involving Protein Kinase A in the visual
245 cortex (Cudmore and Turrigiano, 2004), metabotropic glutamate receptor subtype 5
246 (mGluR5) in the somatosensory cortex, NMDA receptors in the hippocampus (Sourdet et al.,
247 2003; Xu et al., 2005), down-regulation of Kv1 channels in the dorsal lateral geniculate
248 nucleus (Duménieu et al., 2025) or reduction in BK-type calcium-activated potassium
249 currents in the brainstem (Nelson et al., 2003). However, all these changes have ultimately
250 been associated with the modulation (increase or decrease) of intracellular or extracellular
251 calcium, as they are inhibited by calcium chelation. This could also implicate the astrocytic
252 calcium-binding protein S100β, which is strongly expressed in all these plastic regions, and
253 that we demonstrated is required for LTP-IE in the visual cortex. But S100β is much more than
254 a simple Ca^{2+} chelator (Sorci et al., 2010).

255 **S100β: a multifaceted protein**

256 Given that extracellular calcium is a key regulator of all forms of plasticity, S100β, which
257 reduces $[Ca^{2+}]_e$, is expected to have a significant impact on these processes. Surprisingly, our
258 results demonstrated that S100β does not inhibit LTP-IE or AIS plasticity in the visual cortex;

259 rather, it is essential for these processes despite that both have been shown to depend on
260 calcium elevation and Ca^{2+}-activated molecules such as calcineurin and cyclin-dependent
261 kinase 5 (cdk5) (Chand et al., 2015). This underscores the complex and multifaceted role of
262 S100β, which extends beyond calcium regulation. S100β has been shown to interact directly
263 or indirectly with various voltage gated channels, including Ca^{2+}, K^{+}, and Na^{+} channels
264 (Hermann et al., 2012). For example, it facilitates Ca^{2+} flux across artificial membranes,
265 activates L-type Ca^{2+} channels, and inhibits K^{+} channels such as the ether-à-go-go (hEAG1)
266 and Kv4.2 channels (Bancroft et al., 2022). Our previous results demonstrated that S100β
267 enhances the spiking duration and frequency of L5PNs through NaV1.6 potentiation (Ryczko
268 et al., 2021; Gaudel et al., 2025). This is explained by the fact that Na^{+} channels are
269 transiently clogged by Ca^{2+} ions occupying the channel lumen (Armstrong, 1999; Armstrong
270 and Cota, 1999). Notably, LTP-IE requires neurons to fire at approximately 20–30 Hz during
271 the induction protocol. The release of S100β could further promote high-frequency firing and
272 facilitate LTP-IE induction. This idea is further supported by the fact that BAPTA rescues LTP-
273 IE **(Fig S4)**. In addition, activity-dependent relocation of the AIS has been shown to be
274 mediated by T- and L- type calcium channels (Grubb and Burrone, 2010). Similar to what has
275 been described for S100A1, another member of the S100 protein family, S100β could directly
276 bind to L-type calcium channels and increase their opening probability through protein
277 kinase A (PKA) activation (Treves et al., 1997) which is required for LTP-IE activity in the visual
278 cortex (Cudmore and Turrigiano, 2004). S100β secretion is tightly linked to neuronal activity
279 (Nardin et al., 2009), and could serve as a gatekeeper of intrinsic plasticity to allow rapid AIS
280 plasticity in response to high periods of activity, a processus which could be really important
281 during development, especially in the visual cortex (Gutzmann et al., 2014). In addition,
282 S100β could provide a direct mechanism for astrocytes to modulate synaptic plasticity
283 through Ca^{2+} regulation. S100β has long been considered as a direct competitor of
284 calmodulin, another Ca^{2+}-binding protein that plays a key role in synaptic plasticity (Xia and
285 Storm, 2005), which can tilt the balance toward LTD or LTP depending on the level of Ca^{2+}
286 elevation. In line with this idea, S100β perfusion enhanced LTP in the hippocampus
287 (Nishiyama et al., 2002). Taken together, these findings suggest that S100β may also

288 influence other forms of plasticity beyond LTP-IE. Given the well-established interplay
289 between synaptic and intrinsic plasticity (Debanne et al., 2019), it would be interesting to
290 explore whether the interplay between synaptic and intrinsic plasticity involves structural
291 modifications at the AIS, and whether S100β, or other gliotransmitters, act as key mediators
292 of these coordinated forms of plasticity.

293 **S100β, NaV 1.6 and AIS reorganization**

294 Na^+ channels are transiently clogged by Ca^{2+} ions occupying the channel lumen. Reduction
295 of extracellular Ca^{2+} relieves this partial block of the Na^+ channel and allows for a larger influx
296 of Na^+ currents (Armstrong, 1999; Armstrong and Cota, 1999), and an enhanced sodium
297 persistent current (I_{NaP}), which is associated with the control of neuronal excitability and
298 rhythmic activity (Agrawal et al., 2001; Wu et al., 2005). I_{NaP} is most commonly associated to
299 Na^+-channels including the Nav1.6 α-subunit (Drouillas et al., 2023), which is abundantly
300 located at the distal end of the AIS (Van Wart et al., 2007; Hu et al., 2009; Drouillas et al.,
301 2023), where the initiation of APs in L5PNs has been experimentally demonstrated (Palmer
302 and Stuart, 2006), coinciding with the region where we observed structural changes in the
303 AIS in our experiments (**Fig. 1C**). Furthermore, according to computational and experimental
304 analyses, Nav1.6 α-subunits determine the lowest threshold for AP initiation in the distal AIS
305 of cortical pyramidal neurons (Hu et al., 2009). We observed a reduction in the threshold
306 potential for evoking APs (**Fig. 1E**), which could indicate an increase in the density and/or
307 reinsertion of these channels after inducing LTP-IE. The absence of changes in passive cell
308 properties (see Methods) further supports that LTP-IE associated with AIS elongation is
309 mediated by changes in ionic conductances. Molecular trafficking of protein complexes in
310 the AIS can follow two routes during development: (1) either insertion of proteins such as
311 neurofascin 186 (Nfasc186) or the Kv7.3 channel into the somatodendritic and/or axonal
312 membrane followed by bidirectional diffusion until immobilization by interaction with
313 AnkyrinG (AnkG) (Ghosh et al., 2020); or (2) preferential vesicular insertion directly into the
314 AIS, allowing binding to AnkG, as in the case of Nav1.6 (Akin et al., 2015). The maintenance
315 of Nav1.6 channels has not yet been thoroughly studied, but so far, it appears that once
316 anchored, they do not migrate to adjacent membranes. Therefore, although one study

317 showed that prolonged activity caused lateral diffusion of other receptors ($GABA_A$) in the AIS
318 of hippocampal neurons (Muir and Kittler, 2014), we hypothesize that the origin of these
319 structural changes was rather a vesicular insertion of new Nav1.6 channels into the distal AIS
320 minutes after the period of elevated activity. This is consistent with the results of Kuba et al.,
321 (2010), who showed that AIS elongation was accompanied by increased expression of Na^+
322 channels and enhanced axonal I_{NaP} and membrane excitability in the auditory pathway.
323 Moreover, a computational model predicted that the distal AIS exhibits greater variation in
324 terms of Na^+ conductance and that small changes in the density of functional Na^+ channels
325 in this region would have a strong impact on neuronal excitability in L5PNs (Baranauskas et
326 al., 2013). We do not rule out the simultaneous contribution of other VGCCs, such as the
327 combination of T-type and/or L-type VGCCs, which were necessary for activity-dependent
328 AIS relocation (Grubb and Burrone, 2010; Kuba et al., 2015), or K^+ channels, such as Kv7.2,
329 whose activity-dependent expression can increase in the AIS, reducing the shunt current
330 around the AP threshold (Jamann et al., 2021) and enhancing the electrotonic isolation of the
331 distal AIS, a factor that had also been computationally predicted as a key modulator of
332 neuronal excitability (Baranauskas et al., 2013), or Kv2.1, whose phosphorylation,
333 localization in the AIS (non-canonical pathway), and function are regulated by neuronal
334 activity and can drastically affect excitability and intrinsic plasticity (Misonou et al., 2005;
335 Jensen et al., 2017). Even other interactions between key protein partners could have
336 contributed to this activity-driven intrinsic plasticity, such as the phosphorylation of casein
337 kinase 2 (CK2), which regulates the interaction between Na^+ channels and AnkG (Bréchet et
338 al., 2008), or the interaction of Nav1.6 with the microtubule-associated protein Map1b
339 (Mtap1b), which facilitates the trafficking of these channels to the cell surface (O'Brien et al.,
340 2012; Solé et al., 2019). Leveraging the opportunities offered by novel genome-editing
341 techniques and super-resolution microscopy (Willems et al., 2020; Liu et al., 2022), future
342 studies should investigate the exocytic machinery in the AIS in contexts of activity-
343 dependent intrinsic plasticity, perhaps starting with endogenous tagging of Nav1.6 in L5PNs.

344 **AIS plasticity in critical periods**

Brain plasticity driven by activity or experience is enhanced during critical periods. For over 40 years, the primary model for studying critical period plasticity has been the primary visual cortex (Wiesel and Hubel, 1963; Hensch, 2005). Specifically, the critical visual period in mice has been defined from eye opening (P13) to approximately P35. The P13-P19 phase is considered a precritical period, independent of visual experience; P19-P28 represents the critical period with the highest sensitivity to imbalances; and P28-P35 corresponds to the consolidation and closure of the critical period (Gordon and Stryker, 1996; Corlew et al., 2007). Interestingly, the most significant elongation and reduction in AIS development in the visual cortex occur approximately one week before the opening and closing of the critical period, respectively (Gutzmann et al., 2014). This structural refinement of the AIS may be necessary to prepare the cortical network for the subsequent initiation and termination of the critical period. However, what determines the duration of these plasticity windows? GABAergic inhibition has gathered substantial evidence as a key mechanism regulating the onset and duration of the critical period in the visual cortex (Hensch, 2004, 2005). However, it is not the only factor. A recent study demonstrated that astrocytic connexin 30 controls the timing of critical period closure in the visual cortex (Ribot et al., 2021), and remarkably, the reintroduction of immature cultured astrocytes reinstates a period of heightened plasticity in adult animals, resembling the critical visual period (Müller and Best, 1989). Moreover, in other brain regions such as the hippocampus and somatosensory cortex, astrocytes have also been implicated in the closure of the critical plasticity period (Falcón-Moya et al., 2020; Martínez-Gallego et al., 2022). While we have not explored the role of astrocytes in AIS plasticity beyond the visual critical period, it would be interesting to investigate whether astrocytic manipulation could reinstate a period of AIS plasticity in adulthood, when its length is presumed to be stable.

CONCLUSION

The million-dollar question is how astrocytes detect neuronal activity and, more importantly, how they determine when to release the appropriate gliotransmitters, specifically, S100β in this case, at the right time. As previously mentioned, astrocytes can detect neuronal activity through changes in the extracellular ion composition, including K^+, Ca^{2+}, and Na^+. In

374 particular, the sodium/calcium exchanger (NCX) is predominantly expressed in the distal
375 processes and terminal feet of astrocytes and can be easily activated by an increase in
376 astrocytic $[Na^+]i$ driven by neuronal activity. Given that certain astrocytic processes can
377 contact the AIS, it is tempting to speculate that intense neuronal activity increases $[Na^+]_i$
378 signals in astrocytes, allowing Ca^{2+} influx from the extracellular space through the NCX
379 exchanger. In future experiments, it would be interesting to determine whether $[Na^+]_i$ and
380 $[Ca^{2+}]_i$ transients in astrocytes are closely related to specific protocols of intrinsic plasticity.

381 **MATERIAL AND METHODS**

382 **Experimental model**

383 All experiments were conducted in accordance with the rules of the Canadian Institutes of
384 Health Research and were approved by the Animal Care and Use Committee of the University
385 of Montreal (Protocol #23-207). We crossed mice from the newly generated AnkG-GFP-lox
386 knock-in line (B6;129SV-ank3tm1DCI/HD) (Thome et al., 2025) with Vglut2-cre mice
387 (B6J.129S6(FVB)-Slc17a6tm2(cre)Lowl/Mwar). This allowed Cre-dependent expression of
388 AnkG-GFP driven by the VGlut2 promoter, a genetic marker of glutamatergic signaling.
389 VGlut2-AnkG-GFP were fed ad libitum and housed with a 12 h light/dark cycle. Male and
390 female mice were used for experiments.

391 **V1 slice preparation**

392 Coronal slices (350 µm) containing layer 5 of the V1 were prepared from 14- to 30-day-old
393 Vglut2-AnkG-GFP mice. Mice were anesthetized with isoflurane (Pharmaceutical Partners of
394 Canada Inc., Richmond Hill, ON, Canada) and subsequently decapitated. Following
395 decapitation, the skull was quickly removed, and the brain was transferred to modified
396 artificial cerebrospinal fluid (aCSF, in mM: 3 KCl, 1.25 KH2PO4, 4 MgSO4, 26 NaHCO3, 10
397 dextrose, 0.2 CaCl2, 219 sucrose; pH 7.3-7.4, 300-320 mOsmol/kg) that was ice-cold (0-4°C)
398 and oxygenated with a mixture of 95% O2 and 5% CO2. Brain slices were then sectioned
399 using a VT1000S vibratome (Leica). After a 15-minute incubation at 30°C in a temperature-
400 controlled water bath within a slice holder containing oxygenated artificial cerebrospinal
401 fluid (aCSF, in mM: 124 NaCl, 3 KCl, 1.25 KH2PO4, 1.3 MgSO4, 26 NaHCO3, 10 dextrose, and

402 1.2 $CaCl_2$; pH 7.3-7.4, 294-300 mOsmol/kg) bubbled with 95% O_2 and 5% CO_2, slices were
403 transferred to the recording chamber at room temperature. A recovery period of at least one
404 hour was allowed for the slices before recording.
405
406 **Electrophysiology**
407 Recordings were conducted at room temperature in a submerged chamber continuously
408 perfused with artificial CSF (in mM: 124 NaCl, 3 KCl, 1.25 KH_2PO_4, 1.3 $MgSO_4$, 26 $NaHCO_3$,
409 10 dextrose, and 1.2 $CaCl_2$; pH 7.3-7.4, 294-300 mOsmol/kg) bubbled with 95% O_2 and 5%
410 CO_2. Patch microelectrodes were fabricated from borosilicate glass capillaries (1.5 mm
411 outside diameter, 1.12 mm inside diameter, World Precision Instruments) using a P-97 puller
412 (Sutter Instruments). For neuronal recordings, pipettes with resistance ranging from 6 to 12
413 MΩ were filled with an internal solution containing the following (in mM): 140 K-gluconate, 5
414 NaCl, 2 $MgCl_2$, 10 HEPES, 0.5 EGTA, 2 Tris ATP salt, 0.4 Tris GTP salt, pH 7.2-7.3, 280-
415 300mOsmol/kg. To visualize neuronal and axonal morphologies during the experiment, Alexa
416 Fluor 647 was added to the internal solution. Layer 5 pyramidal neurons of the
417 extratelencephalic subtype were selected based on their morphological characteristics
418 (large soma and thick apical dendrite) and electrophysiological properties (burst spiking). All
419 recordings were performed using a Multiclamp 700A amplifier, Digidata 1550B interface
420 coupled to a computer equipped with pClamp 11 software (Molecular Devices, San Jose,
421 CA). After the establishment of a gigaseal, the membrane potential was held at -65 mV, and
422 the membrane patch was ruptured by suction. During the experiments, the changes in Vm
423 (1–6 mV) were corrected by imposing continuous current to maintain the membrane
424 potential constant at -65mV. Recordings were discarded if the resting membrane potential
425 shifted by >6 mV or if resting input resistance (measured with a 50pA hyperpolarizing pulse
426 lasting 50 ms, delivered every 10 seconds) varied >20%. Astrocytes were initially identified
427 morphologically after incubating the slices in the marker Sulforhodamine 101 (SR101) for 5
428 minutes, based on their size and shape. This identification was subsequently confirmed by
429 their electrophysiological characteristics, including a low resting membrane potential and
430 passive responses to negative and positive current injections. For experiments involving

431 astrocyte inactivation, BAPTA tetrapotassium salt (20 mM) was added to the internal solution
432 filling the recording pipette. All recordings were performed in the presence of antagonists
433 of N-methyl-d-aspartate (NMDA), AMPA/kainate, and $GABA_A$ receptors [2-amino-5-
434 phosphonovaleric acid (d-APV), 50 μM; 6-cyano-7-nitroquinoxalene-2,3-dione (CNQX), 20
435 μM; and Gabazine, 20 μM, respectively, which were all purchased from Tocris Biosciences
436 (Ellisville, Missouri, USA)].
437
438 **Plasticity Protocol and Analysis**
439 After achieving whole-cell access by rupturing the membrane with negative pressure, a
440 waiting period of 5 to 10 minutes was allowed for the cell to dialyze with the pipette solution
441 and for the Alexa 647 fluorescent dye to diffuse. Throughout the recording, intrinsic
442 excitability was assessed every 10 seconds using a small, constant-amplitude depolarizing
443 pulse (500 ms, 10–60 pA), which was selected to evoke 2–3 APs during the baseline period (5
444 minutes) and then maintained constant throughout the recording. To generate input-output
445 curves and determine the current threshold for AP generation, a series of depolarizing
446 current injections (0–100 pA in 10 pA increments) was applied before the baseline period and
447 at the end of the recording. Each series was delivered at least twice per cell, and responses
448 were averaged. The induction stimulus consisted of 500 ms depolarizing pulses (150–180 pA)
449 delivered 60 times at 4-second intervals, with an amplitude selected to evoke a sustained
450 firing rate of 18–30 Hz. Only neurons with a stable baseline, consistent recording parameters,
451 and a post-induction recording duration of at least 20 minutes were included in the analysis.
452 The degree of LTP-IE was calculated as the ratio of firing frequency during the last 10 minutes
453 of the post-induction recording to the baseline. Intra- and intercellular comparisons were
454 performed by extracting the average response per minute (6 pulses every 15 seconds), and
455 the mean firing rate during the 5-minute baseline period was used to normalize data before
456 and after induction. Control cells remained at rest during the induction stimulus period, and
457 analyses were conducted similarly in this condition.
458
459 **Optogenetic Stimulation**

460 Astrocytes peri-AIS in VGlut2-AnkG-GFP mice, which received bilateral intracerebral viral
461 administration at P0 of an AAV2/5-GFAP-hChR2(H134R)-mCherry (3.40E+12) expressing
462 GFAP-promoter-driven Channelrhodopsin-2 (ChR2) fused to the mCherry reporter (provided
463 by the CNP Viral Vector Core at the CERVO Research Center, RRID: SCR_016477), were
464 optogenetically stimulated (beginning two weeks after viral injection) using two lasers (440
465 nm and 488 nm) simultaneously in the SIM light path of an FV1000 microscope (Olympus).
466 The SIM scanner was used in square scanning mode to photoactivate small manually
467 delineated areas within astrocytes near the AIS of the recorded neurons. Optogenetic
468 stimulations were applied after the baseline period using 60 pulses of 2 s ON and 2 s OFF
469 (10–20% laser power / 8.6–14.9 μW for the 440 nm laser / 8.7–15.9 μW for the 488 nm laser).
470 To assess the efficacy of the stimulation, laser pulses were applied while recording the
471 electrophysiological activity of astrocytes. These recordings confirmed that the
472 photostimulation reliably evoked small membrane depolarizations, averaging 7.4 mV and
473 ranging between 6 and 9 mV.
474
475 **Drugs**
476 Chemicals used in this study were purchased from Sigma-Aldrich (Oakville, Ontario,
477 Canada), Tocris Biosciences (Ellisville, Missouri, USA) and Abcam (Cambridge, UK). The
478 following drugs were bath-applied using a syringe pump: D,L-2-amino-5-phosphonovaleric
479 acid (APV, 75 μM), CNQX (10 μM), SR 95531 hydrobromide (Gabazine, 20 μM) and Suramin
480 (100 μM). In some experiments, the Ca^{2+}-binding protein S100β (129 μM) (Produced in the
481 Department of Biochemistry of the Université de Montreal as described in Morquette et al.,
482 2015) or 1,2-bis(o-aminophenoxy) ethane-N,N,N',N'-tetraacetic acid tetrasodium salt
483 (BAPTA, 5 mM) were locally applied using glass micropipettes (tip diameter ~1 μm) with 2–20
484 psi pressure pulses for 5 minutes (Picospritzer III, Parker Instrumentation, Fairfield, NJ, USA).
485 Monoclonal anti-S100β antibodies (mouse anti-S100β, Sigma Aldrich #S2532 or rabbit anti-
486 S100β, Abcam ab56642), as well as their denatured form, were applied locally with large-tip
487 (10-20 μm) glass micropipettes carefully lowered near the AIS recorded neuron with 0.1-2 psi
488 pressure pulses lasting 5 minutes. All bath-applied chemicals were diluted in water at 100X

489 their final concentrations and further diluted through the perfusing aCSF at their final
490 concentrations.
491
492 **Immunohistochemistry and confocal microscopy**
493 For the immunohistochemistry against AnkG and NeuN, coronal brainstem slices (350 µm)
494 were prepared from 14 to 30-day-old VGlut2-AnkG-GFP mice using a vibratome VT 1000S
495 (Leica), immediately immersed in a solution of 4% (wt/vol) paraformaldehyde in PBS, and
496 kept for one hour at 4°C. The sections were rinsed 3 times for 10 minutes in PBS and
497 incubated in a blocking solution containing 0.3% Triton X-100 and 5% Normal Donkey Serum
498 (Jackson ImmunoResearch #017-000-121) in PBS for one hour at room temperature. The
499 sections were then rinsed 3 times for 10 minutes in PBS and incubated overnight at 4°C in a
500 mix of the primary antibodies (chicken anti-AnkG, EnCor Biotech #PCAC-ANK3, dilution
501 1:1000; mouse anti-NeuN, Millipore #MAB377, dilution 1:500). The following day, the slices
502 were rinsed 5 times for 10 minutes in PBS and incubated in the relevant secondary antibodies
503 mix (donkey anti-chicken Alexa Fluor 647, Jackson Immunoresearch #703-605-155, dilution
504 1:250; donkey anti-mouse Alexa Fluor 594, Jackson Immunoresearch #715-585-151, dilution
505 1:250) diluted in the blocking solution for 120 minutes in a dark chamber at room
506 temperature. The sections were then rinsed 4 times for 15 minutes in PBS and mounted on
507 ColorFrost Plus slides (Fisher Scientific, Ottawa, Ontario, Canada) using Fluoromount-G
508 (Southern Biotech, Birmingham, Alabama, USA). A similar procedure was used for the
509 immunohistochemistry against S100β, except that the slices were immersed in 4% (wt/vol)
510 paraformaldehyde in PBS overnight at 4°C. The staining was performed using mouse anti-
511 S100β (Sigma #S2532, 1:400) as the primary antibody and donkey anti-mouse Alexa Fluor
512 647 (Abcam #ab150107, 1:250) as the secondary antibody. The washing steps, blocking
513 conditions, and mounting procedure were identical to those described above. Slides imaging
514 was performed using either a Zeiss LSM-900 Confocal Airyscan microscope or an FV1000
515 confocal microscope (Olympus). AnkG-GFP was visualized in real-time during
516 electrophysiology experiments using the FV1000, operated with FV10-ASW imaging software
517 (Version 03.00). Z-stacks were acquired at a speed of 10 µs/pixel and a resolution of 800 ×

800 pixels, with 1 µm step sizes and a zoom range of 2 to 4×. To minimize phototoxicity and photobleaching, AIS z-stacks were captured at two time points: 5 minutes before induction or drug exposure, as applicable, and 30 minutes afterward. AIS length was measured manually and by fluorescence intensity along a 1-pixel-wide line drawn from the soma down the axon (1 pixel ≈ 0.206 µm), using Fiji software (ImageJ 1.50e, NIH, USA). Fluorescence profiles were smoothed using a 10-point (~2 µm) sliding mean and normalized between 1 (maximum) and 0 (minimum). The AIS end was defined at a 33% fluorescence threshold (method adapted from Grubb and Burrone, 2010). No difference was observed between the two methods. In a subset of experiments (**Fig. S1**), images were acquired using a two-photon microscope equipped with a polygon scanner (BliQ Photonics), enabling high-speed imaging while minimizing phototoxicity from repeated AIS imaging during recording.

Quantification and statical analysis

Data are presented as mean ± standard error to the mean (SEM) and as proportions (%). Statistical analyses were performed depending on the experimental design. All paired comparisons before and after treatment were confirmed to follow a normal distribution (Shapiro–Wilk test, $P>0.05$) and were analyzed using paired t-tests. Comparisons between independent groups, for which normality could not be assumed, were performed using the non-parametric Mann–Whitney U test. Statistical significance was set at *$P<0.05$, **$P<0.01$, and ***$P<0.001$; NS indicates not significant. Data analysis was performed using SPSS (IBM SPSS Statistics).

DECLARATIONS

Author contributions

R.S.G., Y.I and A.K wrote the paper. R.S.G and Y.I collected and analyzed the data and built the figures. All authors contributed to the article and approved the submitted version.

Acknowledgements

We thank Dr. Dorly Verdier for critically reading a preliminary version of the manuscript and members of A.K laboratories for comments on the manuscript and technical support. We are especially grateful to our esteemed colleagues, Dr. James G. Omichinski and Dr. Haytham Wahba, from the Department of Biochemistry at the Université de Montréal, for their invaluable contribution to the production of the S100β protein.

Funding

This work was supported by the Canadian Institutes of Health Research (Grant # 197855), Natural Sciences and Engineering Research Council of Canada (RGPIN/05255-2020), CIRCA Post-doctoral fellowship to Y.I.

Conflict of Interest Statement

The authors declare that the research was conducted in the absence of any commercial or financial relationships that could be construed as a potential conflict of interest.

Availability of data and materials

All data generated or analysed during this study are included in this published article.

Preprint

This manuscript was posted on a preprint.

REFERENCES

Agrawal, N., Hamam, B. N., Magistretti, J., Alonso, A., and Ragsdale, D. S. (2001). Persistent sodium channel activity mediates subthreshold membrane potential oscillations and low-threshold spikes in rat entorhinal cortex layer V neurons. *Neuroscience* 102, 53–64. doi: 10.1016/S0306-4522(00)00455-3

Akin, E. J., Solé, L., Dib-Hajj, S. D., Waxman, S. G., and Tamkun, M. M. (2015). Preferential Targeting of Nav1.6 Voltage-Gated Na+ Channels to the Axon Initial Segment during Development. *PLOS ONE* 10, e0124397. doi: 10.1371/journal.pone.0124397

Andersson, M., Blomstrand, F., and Hanse, E. (2007). Astrocytes play a critical role in transient heterosynaptic depression in the rat hippocampal CA1 region. *The Journal of Physiology* 585, 843–852. doi: 10.1113/jphysiol.2007.142737

572 Araque, A., Parpura, V., Sanzgiri, R. P., and Haydon, P. G. (1998). Glutamate-dependent astrocyte
573 modulation of synaptic transmission between cultured hippocampal neurons. *European Journal of*
574 *Neuroscience* 10, 2129–2142. doi: 10.1046/j.1460-9568.1998.00221.x

575 Armstrong, C. M. (1999). Distinguishing surface effects of calcium ion from pore-occupancy effects
576 in Na+ channels. *Proceedings of the National Academy of Sciences* 96, 4158–4163. doi:
577 10.1073/pnas.96.7.4158

578 Armstrong, C. M., and Cota, G. (1999). Calcium block of Na+ channels and its effect on closing rate.
579 *Proceedings of the National Academy of Sciences* 96, 4154–4157. doi: 10.1073/pnas.96.7.4154

580 Bancroft, E. A., De La Mora, M., Pandey, G., Zarate, S. M., and Srinivasan, R. (2022). Extracellular
581 S100B inhibits A-type voltage-gated potassium currents and increases L-type voltage-gated calcium
582 channel activity in dopaminergic neurons. *Glia* 70, 2330–2347. doi: 10.1002/glia.24254

583 Baranauskas, G., David, Y., and Fleidervish, I. A. (2013). Spatial mismatch between the Na^+ flux and
584 spike initiation in axon initial segment. *Proceedings of the National Academy of Sciences* 110, 4051–
585 4056. doi: 10.1073/pnas.1215125110

586 Benitez, M. J., Retana, D., Ordoñez-Gutiérrez, L., Colmena, I., Goméz, M. J., Álvarez, R., et al. (2024).
587 Transcriptomic alterations in APP/PS1 mice astrocytes lead to early postnatal axon initial segment
588 structural changes. *Cell. Mol. Life Sci.* 81, 444. doi: 10.1007/s00018-024-05485-9

589 Bréchet, A., Fache, M.-P., Brachet, A., Ferracci, G., Baude, A., Irondelle, M., et al. (2008). Protein
590 kinase CK2 contributes to the organization of sodium channels in axonal membranes by regulating
591 their interactions with ankyrin G. *Journal of Cell Biology* 183, 1101–1114. doi:
592 10.1083/jcb.200805169

593 Campanac, E., and Debanne, D. (2007). Plasticity of neuronal excitability: Hebbian rules beyond the
594 synapse. *Arch Ital Biol* 145, 277–287.

595 Campanac, E., and Debanne, D. (2008). Spike timing-dependent plasticity: a learning rule for
596 dendritic integration in rat CA1 pyramidal neurons. *The Journal of Physiology* 586, 779–793. doi:
597 10.1113/jphysiol.2007.147017

598 Chand, A. N., Galliano, E., Chesters, R. A., and Grubb, M. S. (2015). A Distinct Subtype of
599 Dopaminergic Interneuron Displays Inverted Structural Plasticity at the Axon Initial Segment. *J.*
600 *Neurosci.* 35, 1573–1590. doi: 10.1523/JNEUROSCI.3515-14.2015

601 Corlew, R., Wang, Y., Ghermazien, H., Erisir, A., and Philpot, B. D. (2007). Developmental Switch in
602 the Contribution of Presynaptic and Postsynaptic NMDA Receptors to Long-Term Depression. *J.*
603 *Neurosci.* 27, 9835–9845. doi: 10.1523/JNEUROSCI.5494-06.2007

604 Cudmore, R. H., and Turrigiano, G. G. (2004). Long-Term Potentiation of Intrinsic Excitability in LV
605 Visual Cortical Neurons. *Journal of Neurophysiology* 92, 341–348. doi: 10.1152/jn.01059.2003

606 Debanne, D., Campanac, E., Bialowas, A., Carlier, E., and Alcaraz, G. (2011). Axon Physiology.
607 *Physiological Reviews*. doi: 10.1152/physrev.00048.2009

Debanne, D., Inglebert, Y., and Russier, M. (2019). Plasticity of intrinsic neuronal excitability. *Current Opinion in Neurobiology* 54, 73–82. doi: 10.1016/j.conb.2018.09.001

Debanne, D., and Rama, S. (2011). Astrocytes Shape Axonal Signaling. *Science Signaling* 4, pe11–pe11. doi: 10.1126/scisignal.2001884

Debanne, D., and Russier, M. (2019). The contribution of ion channels in input-output plasticity. *Neurobiology of Learning and Memory* 166, 107095. doi: 10.1016/j.nlm.2019.107095

Donato, R., Sorci, G., Riuzzi, F., Arcuri, C., Bianchi, R., Brozzi, F., et al. (2009). S100B's double life: Intracellular regulator and extracellular signal. *Biochimica et Biophysica Acta (BBA) - Molecular Cell Research* 1793, 1008–1022. doi: 10.1016/j.bbamcr.2008.11.009

Drouillas, B., Brocard, C., Zanella, S., Bos, R., and Brocard, F. (2023). Persistent Nav1.1 and Nav1.6 currents drive spinal locomotor functions through nonlinear dynamics. *Cell Reports* 42, 113085. doi: 10.1016/j.celrep.2023.113085

Duménieu, M., Fronzaroli-Molinieres, L., Naudin, L., Iborra-Bonnaure, C., Wakade, A., Zanin, E., et al. (2025). Visual activity enhances neuronal excitability in thalamic relay neurons. *Science Advances* 11, eadp4627. doi: 10.1126/sciadv.adp4627

Evans, M. D., Dumitrescu, A. S., Kruijssen, D. L. H., Taylor, S. E., and Grubb, M. S. (2015). Rapid Modulation of Axon Initial Segment Length Influences Repetitive Spike Firing. *Cell Reports* 13, 1233–1245. doi: 10.1016/j.celrep.2015.09.066

Evans, M. D., Sammons, R. P., Lebron, S., Dumitrescu, A. S., Watkins, T. B. K., Uebele, V. N., et al. (2013). Calcineurin Signaling Mediates Activity-Dependent Relocation of the Axon Initial Segment. *J. Neurosci.* 33, 6950–6963. doi: 10.1523/JNEUROSCI.0277-13.2013

Falcón-Moya, R., Pérez-Rodríguez, M., Prius-Mengual, J., Andrade-Talavera, Y., Arroyo-García, L. E., Pérez-Artés, R., et al. (2020). Astrocyte-mediated switch in spike timing-dependent plasticity during hippocampal development. *Nat Commun* 11, 4388. doi: 10.1038/s41467-020-18024-4

Forsberg, M., Seth, H., Björefeldt, A., Lyckenvik, T., Andersson, M., Wasling, P., et al. (2019). Ionized calcium in human cerebrospinal fluid and its influence on intrinsic and synaptic excitability of hippocampal pyramidal neurons in the rat. *Journal of Neurochemistry* 149, 452–470. doi: 10.1111/jnc.14693

Forsberg, M., Zhou, D., Jalali, S., Faravelli, G., Seth, H., Björefeldt, A., et al. (2025). Evaluation of mechanisms involved in regulation of intrinsic excitability by extracellular calcium in CA1 pyramidal neurons of rat. *Journal of Neurochemistry* 169, e16209. doi: 10.1111/jnc.16209

Fréal, A., Jamann, N., Ten Bos, J., Jansen, J., Petersen, N., Ligthart, T., et al. (2023). Sodium channel endocytosis drives axon initial segment plasticity. *Science Advances* 9, eadf3885. doi: 10.1126/sciadv.adf3885

Gaudel, F., Giraud, J., Morquette, P., Couillard-Larocque, M., Verdier, D., and Kolta, A. (2025). Astrocyte-induced firing in primary afferent axons. *iScience* 0. doi: 10.1016/j.isci.2025.112006

Ghosh, A., Malavasi, E. L., Sherman, D. L., and Brophy, P. J. (2020). Neurofascin and Kv7.3 are delivered to somatic and axon terminal surface membranes en route to the axon initial segment. *eLife* 9, e60619. doi: 10.7554/eLife.60619

Gordon, J. A., and Stryker, M. P. (1996). Experience-Dependent Plasticity of Binocular Responses in the Primary Visual Cortex of the Mouse. *J. Neurosci.* 16, 3274–3286. doi: 10.1523/JNEUROSCI.16-10-03274.1996

Grubb, M. S., and Burrone, J. (2010). Activity-dependent relocation of the axon initial segment fine-tunes neuronal excitability. *Nature* 465, 1070–1074. doi: 10.1038/nature09160

Grubb, M. S., Shu, Y., Kuba, H., Rasband, M. N., Wimmer, V. C., and Bender, K. J. (2011). Short- and long-term plasticity at the axon initial segment. *J Neurosci* 31, 16049–16055. doi: 10.1523/JNEUROSCI.4064-11.2011

Gutzmann, A., Erguel, N., Grossmann, R., Schultz, C., Wahle, P., and Engelhardt, M. (2014). A period of structural plasticity at the axon initial segment in developing visual cortex. *Front. Neuroanat.* 8. doi: 10.3389/fnana.2014.00011

Hensch, T. K. (2004). Critical period regulation. *Annu Rev Neurosci* 27, 549–579. doi: 10.1146/annurev.neuro.27.070203.144327

Hensch, T. K. (2005). Critical period plasticity in local cortical circuits. *Nat Rev Neurosci* 6, 877–888. doi: 10.1038/nrn1787

Hermann, A., Donato, R., Weiger, T. M., and Chazin, W. J. (2012). S100 Calcium Binding Proteins and Ion Channels. *Front Pharmacol* 3, 67. doi: 10.3389/fphar.2012.00067

Höfflin, F., Jack, A., Riedel, C., Mack-Bucher, J., Roos, J., Corcelli, C., et al. (2017). Heterogeneity of the Axon Initial Segment in Interneurons and Pyramidal Cells of Rodent Visual Cortex. *Front. Cell. Neurosci.* 11. doi: 10.3389/fncel.2017.00332

Hu, W., Tian, C., Li, T., Yang, M., Hou, H., and Shu, Y. (2009). Distinct contributions of Nav1.6 and Nav1.2 in action potential initiation and backpropagation. *Nat Neurosci* 12, 996–1002. doi: 10.1038/nn.2359

Inglebert, Y., Aljadeff, J., Brunel, N., and Debanne, D. (2020). Synaptic plasticity rules with physiological calcium levels. *Proceedings of the National Academy of Sciences* 117, 33639–33648. doi: 10.1073/pnas.2013663117

Jamann, N., Dannehl, D., Lehmann, N., Wagener, R., Thielemann, C., Schultz, C., et al. (2021). Sensory input drives rapid homeostatic scaling of the axon initial segment in mouse barrel cortex. *Nat Commun* 12, 23. doi: 10.1038/s41467-020-20232-x

Jensen, C. S., Watanabe, S., Stas, J. I., Klaphaak, J., Yamane, A., Schmitt, N., et al. (2017). Trafficking of Kv2.1 Channels to the Axon Initial Segment by a Novel Nonconventional Secretory Pathway. *J. Neurosci.* 37, 11523–11536. doi: 10.1523/JNEUROSCI.3510-16.2017

Kuba, H., Ishii, T. M., and Ohmori, H. (2006). Axonal site of spike initiation enhances auditory coincidence detection. *Nature* 444, 1069–1072. doi: 10.1038/nature05347

Kuba, H., Oichi, Y., and Ohmori, H. (2010). Presynaptic activity regulates Na+ channel distribution at the axon initial segment. *Nature* 465, 1075–1078. doi: 10.1038/nature09087

Kuba, H., Yamada, R., Ishiguro, G., and Adachi, R. (2015). Redistribution of Kv1 and Kv7 enhances neuronal excitability during structural axon initial segment plasticity. *Nat Commun* 6, 8815. doi: 10.1038/ncomms9815

Leterrier, C. (2018). The Axon Initial Segment: An Updated Viewpoint. *J Neurosci* 38, 2135–2145. doi: 10.1523/JNEUROSCI.1922-17.2018

Lezmy, J., Arancibia-Cárcamo, I. L., Quintela-López, T., Sherman, D. L., Brophy, P. J., and Attwell, D. (2021). Astrocyte Ca2+-evoked ATP release regulates myelinated axon excitability and conduction speed. *Science* 374, eabh2858. doi: 10.1126/science.abh2858

Liu, H., Wang, H.-G., Pitt, G., and Liu, Z. (2022). Direct Observation of Compartment-Specific Localization and Dynamics of Voltage-Gated Sodium Channels. *J Neurosci* 42, 5482–5498. doi: 10.1523/JNEUROSCI.0086-22.2022

Martínez-Gallego, I., Pérez-Rodríguez, M., Coatl-Cuaya, H., Flores, G., and Rodríguez-Moreno, A. (2022). Adenosine and Astrocytes Determine the Developmental Dynamics of Spike Timing-Dependent Plasticity in the Somatosensory Cortex. *J Neurosci* 42, 6038–6052. doi: 10.1523/JNEUROSCI.0115-22.2022

Misonou, H., Mohapatra, D. P., and Trimmer, J. S. (2005). Kv2.1: A Voltage-Gated K+ Channel Critical to Dynamic Control of Neuronal Excitability. *NeuroToxicology* 26, 743–752. doi: 10.1016/j.neuro.2005.02.003

Morquette, P., Verdier, D., Kadala, A., Féthière, J., Philippe, A. G., Robitaille, R., et al. (2015). An astrocyte-dependent mechanism for neuronal rhythmogenesis. *Nat Neurosci* 18, 844–854. doi: 10.1038/nn.4013

Muir, J., and Kittler, J. T. (2014). Plasticity of GABAA receptor diffusion dynamics at the axon initial segment. *Front. Cell. Neurosci.* 8. doi: 10.3389/fncel.2014.00151

Müller, C. M., and Best, J. (1989). Ocular dominance plasticity in adult cat visual cortex after transplantation of cultured astrocytes. *Nature* 342, 427–430. doi: 10.1038/342427a0

Nardin, P., Tortorelli, L., Quincozes-Santos, A., de Almeida, L. M. V., Leite, M. C., Thomazi, A. P., et al. (2009). S100B Secretion in Acute Brain Slices: Modulation by Extracellular Levels of Ca2+ and K+. *Neurochem Res* 34, 1603–1611. doi: 10.1007/s11064-009-9949-0

Nataraj, K., Le Roux, N., Nahmani, M., Lefort, S., and Turrigiano, G. (2010). Visual Deprivation Suppresses L5 Pyramidal Neuron Excitability by Preventing the Induction of Intrinsic Plasticity. *Neuron* 68, 750–762. doi: 10.1016/j.neuron.2010.09.033

Nelson, A. B., Krispel, C. M., Sekirnjak, C., and du Lac, S. (2003). Long-lasting increases in intrinsic excitability triggered by inhibition. *Neuron* 40, 609–620. doi: 10.1016/s0896-6273(03)00641-x

Nishiyama, H., Knopfel, T., Endo, S., and Itohara, S. (2002). Glial protein S100B modulates long-term neuronal synaptic plasticity. *Proc Natl Acad Sci U S A* 99, 4037–4042. doi: 10.1073/pnas.052020999

O'Brien, J. E., Sharkey, L. M., Vallianatos, C. N., Han, C., Blossom, J. C., Yu, T., et al. (2012). Interaction of Voltage-gated Sodium Channel Nav1.6 (SCN8A) with Microtubule-associated Protein Map1b *. *Journal of Biological Chemistry* 287, 18459–18466. doi: 10.1074/jbc.M111.336024

Palmer, L. M., and Stuart, G. J. (2006). Site of Action Potential Initiation in Layer 5 Pyramidal Neurons. *J. Neurosci.* 26, 1854–1863. doi: 10.1523/JNEUROSCI.4812-05.2006

Ribot, J., Breton, R., Calvo, C.-F., Moulard, J., Ezan, P., Zapata, J., et al. (2021). Astrocytes close the mouse critical period for visual plasticity. *Science* 373, 77–81. doi: 10.1126/science.abf5273

Ryczko, D., Hanini-Daoud, M., Condamine, S., Bréant, B. J. B., Fougère, M., Araya, R., et al. (2021). S100β-mediated astroglial control of firing and input processing in layer 5 pyramidal neurons of the mouse visual cortex. *The Journal of Physiology* 599, 677–707. doi: 10.1113/JP280501

Sanz-Gálvez, R., Falardeau, D., Kolta, A., and Inglebert, Y. (2024). The role of astrocytes from synaptic to non-synaptic plasticity. *Front. Cell. Neurosci.* 18. doi: 10.3389/fncel.2024.1477985

Schlüter, A., Del Turco, D., Deller, T., Gutzmann, A., Schultz, C., and Engelhardt, M. (2017). Structural Plasticity of Synaptopodin in the Axon Initial Segment during Visual Cortex Development. *Cerebral Cortex* 27, 4662–4675. doi: 10.1093/cercor/bhx208

Solé, L., Wagnon, J. L., Akin, E. J., Meisler, M. H., and Tamkun, M. M. (2019). The MAP1B Binding Domain of Nav1.6 Is Required for Stable Expression at the Axon Initial Segment. *J. Neurosci.* 39, 4238–4251. doi: 10.1523/JNEUROSCI.2771-18.2019

Sorci, G., Riuzzi, F., Arcuri, C., Bianchi, R., Brozzi, F., Tubaro, C., et al. (2010). The many faces of S100B protein: when an extracellular factor inactivates its own receptor and activates another one. *Ital J Anat Embryol* 115, 147–151.

Sourdet, V., Russier, M., Daoudal, G., Ankri, N., and Debanne, D. (2003). Long-term enhancement of neuronal excitability and temporal fidelity mediated by metabotropic glutamate receptor subtype 5. *J Neurosci* 23, 10238–10248. doi: 10.1523/JNEUROSCI.23-32-10238.2003

Thome, C., Janssen, J. M., Karabulut, S., Acuna, C., D'Este, E., Soyka, S. J., et al. (2025). Live imaging of excitable axonal microdomains in ankyrin-G-GFP mice. *eLife* 12, RP87078. doi: 10.7554/eLife.87078

Treves, S., Scutari, E., Robert, M., Groh, S., Ottolia, M., Prestipino, G., et al. (1997). Interaction of S100A1 with the Ca2+ Release Channel (Ryanodine Receptor) of Skeletal Muscle. *Biochemistry* 36, 11496–11503. doi: 10.1021/bi970160w

Van Wart, A., Trimmer, J. S., and Matthews, G. (2007). Polarized distribution of ion channels within microdomains of the axon initial segment. *Journal of Comparative Neurology* 500, 339–352. doi: 10.1002/cne.21173

Watanabe, A., Guo, C., and Sjöström, P. J. (2023). The developmental profile of visual cortex astrocytes. *iScience* 26, 106828. doi: 10.1016/j.isci.2023.106828

Wiesel, T. N., and Hubel, D. H. (1963). Single-cell responses in striate cortex of kittens deprived of vision in one eye. *Journal of Neurophysiology* 26, 1003–1017. doi: 10.1152/jn.1963.26.6.1003

755 Willems, J., Jong, A. P. H. de, Scheefhals, N., Mertens, E., Catsburg, L. A. E., Poorthuis, R. B., et al.
756 (2020). ORANGE: A CRISPR/Cas9-based genome editing toolbox for epitope tagging of endogenous
757 proteins in neurons. *PLOS Biology* 18, e3000665. doi: 10.1371/journal.pbio.3000665

758 Wu, N., Enomoto, A., Tanaka, S., Hsiao, C.-F., Nykamp, D. Q., Izhikevich, E., et al. (2005). Persistent
759 Sodium Currents in Mesencephalic V Neurons Participate in Burst Generation and Control of
760 Membrane Excitability. *Journal of Neurophysiology* 93, 2710–2722. doi: 10.1152/jn.00636.2004

761 Xia, Z., and Storm, D. R. (2005). The role of calmodulin as a signal integrator for synaptic plasticity.
762 *Nat Rev Neurosci* 6, 267–276. doi: 10.1038/nrn1647

763 Xu, J., Kang, N., Jiang, L., Nedergaard, M., and Kang, J. (2005). Activity-Dependent Long-Term
764 Potentiation of Intrinsic Excitability in Hippocampal CA1 Pyramidal Neurons. *J. Neurosci.* 25, 1750–
765 1760. doi: 10.1523/JNEUROSCI.4217-04.2005

766 Yamada, R., and Kuba, H. (2016). Structural and Functional Plasticity at the Axon Initial Segment.
767 *Front. Cell. Neurosci.* 10. doi: 10.3389/fncel.2016.00250

768 Yang, Y., Ge, W., Chen, Y., Zhang, Z., Shen, W., Wu, C., et al. (2003). Contribution of astrocytes to
769 hippocampal long-term potentiation through release of d-serine. *Proceedings of the National*
770 *Academy of Sciences* 100, 15194–15199. doi: 10.1073/pnas.2431073100

771

772 **FIGURE LEGENDS**

773 **Figure 1. LTP-IE is associated with rapid AIS plasticity**

774 **A.** *Top*. High-resolution images showing strong co-localization of AnkG (red, *left*) and GFP
775 (green, *middle*) in pyramidal neurons (cyan, *right*) from layer 5 (L5PNs) of the visual cortex.
776 *Bottom left.* Photomicrography of the axon initial segment (AIS) (AnkG-GFP) in L5PNs filled
777 with Alexa 647. *Bottom right.* Membrane response of the whole-cell recorded neuron at the
778 soma during the induction protocol. **B.** *Left*. Time course of normalized spike number before
779 and after (representative traces shown above) induction (red) and in control conditions
780 (black). *Right*. Quantification of spike number changes in the last 10 minutes, with individual
781 values for each cell represented as red (induction) and black (control) open circles. **C.** *Left*.
782 Live image of an AnkG-GFP-positive neuron filled with Alexa Fluor 647 before and after
783 induction. Black arrowheads indicate the start and end of the AIS. *Middle*. Induction of
784 intrinsic excitability potentiation elongates AIS length (left, manual measurement of
785 individual cells; right, mean normalized fluorescence intensity profiles before (black) and 30
786 min after induction (red). Arrowheads indicate AIS end positions where the fluorescence

profile crosses the 33% threshold, showing AIS elongation). **D.** *Left*. Current-number of spike relationships for each condition (before and after induction). Induction caused a leftward shift in the mean curve. *Right*. Representative traces of individual current injections at different amplitudes. Note the difference in the spike number with the same amplitude before and after induction. **E.** Decrease in Rheobase after induction. **F.** *Left*. Live image of an AnkG-GFP-positive neuron fixed with Alexa Fluor 647 before and after the control condition. Black arrowheads indicate the start and end of the AIS. *Middle*. No AIS length change conditions (left: manual measurements; right: fluorescence profiles before and after control, with no shift at the 33% threshold). **G.** *Left*. Current-number of spike relationships for each condition (before and after the control period). No shift in the mean curve was observed. *Right*. Representative traces of individual current injections at different amplitudes in the control condition, with no changes observed. **H.** No change in Rheobase in the control condition.

Figure 2. Astrocytic inactivation prevents LTP-IE and AIS plasticity

A. Confocal imaging of Sulforhodamine (SR101) labeling in astrocytes of layer 5 of the visual cortex. **B.** *Left*. Experimental paradigm. Stimulation was performed by current injection into the whole-cell recorded neuron, after targeting a neighboring peri-AIS astrocyte for recording with a BAPTA filled pipette for its inactivation. *Middle*. Time course of normalized spike number before and after induction (red) and during peri-AIS astrocyte network inactivation (green), with representative traces shown above. *Right*. Quantification of spike number changes in the last 10 minutes, with individual values for each cell represented as red (induction) and green (astrocytes inactivated) open circles and distance of the inactivated astrocytes from the soma of the recorded neuron. **C.** Live image of an AnkG-GFP-positive neuron filled with Alexa Fluor 647 before and after induction during peri-AIS astrocyte network inactivation, filled with Alexa Fluor 594. Black arrowheads indicate the start and end of the AIS. *Right*. Peri-AIS astrocyte inactivation prevented the change in AIS length. **D.** *Left*. Current-number of spike relationships for each condition (before and after induction during

815 peri-AIS astrocyte network inactivation). No shift in the mean curve was observed. *Right*.
816 Representative traces of individual current injections at different amplitudes, with no
817 changes observed. **E.** No change in Rheobase in the recorded neuron during peri-AIS
818 astrocyte network inactivation.

819

820 **Figure 3. Blockade of the astrocytic protein S100β impairs LTP-IE and AIS plasticity**

821 **A.** *Left*. Experimental paradigm. The induction protocol was performed by current injection
822 into the whole-cell recorded neuron 5 minutes after a local application of either an S100β
823 antibody or its denatured form. *Middle*. Time course of normalized spike number before and
824 after induction, with prior application of S100β antibody (purple) and its denatured form
825 (pink), with representative traces shown above. *Right*. Quantification of spike number
826 changes in the last 10 minutes, with individual values for each cell represented as purple
827 (S100β antibody) and pink (S100β antibody denatured) open circles. **B.** *Left*. Live image of an
828 AnkG-GFP-positive neuron filled with Alexa Fluor 647 before and after the application of
829 S100β antibody, followed by the induction protocol. Black arrowheads indicate the start and
830 end of the AIS. *Right*. The application of the S100β antibody, prior to induction, prevents the
831 change in AIS length. **C.** *Left*. Current-number of spike relationships for each condition
832 (before and after S100β antibody application, followed by the induction protocol). Induction
833 caused a rightward shift in the mean curve. *Right*. Representative traces of individual current
834 injections at different amplitudes. Note the difference in the spike number with the same
835 amplitude before and after induction with prior application of S100β antibody. **D.** No change
836 in Rheobase in the recorded neuron with the application of S100β antibody prior to induction.
837 **E.** *Left*. Live image of an AnkG-GFP-positive neuron filled with Alexa Fluor 647 before and after
838 the application of S100β antibody denatured, followed by the induction protocol. *Right*. The
839 application of denatured S100β antibody prior to induction does not prevent the change in
840 AIS length. **F.** *Left*. Current-number of spike relationships for each condition (before and after
841 S100β antibody denatured application, followed by the induction protocol). Induction
842 caused a leftward shift in the mean curve. *Right*. Representative traces of individual current

843 injections at different amplitudes. Note the difference in the spike number with the same
844 amplitude before and after induction with prior application of S100β antibody denatured. **G.**
845 No change in Rheobase in the recorded neuron with the application of S100β antibody
846 denatured prior to induction.

847

848 **Figure 4. Optogenetic activation of peri-AIS astrocyte reproduces LTP-IE and AIS**
849 **plasticity**

850 **A.** *Left*. Schematic representation of the strategy used for the optogenetic activation of
851 astrocytes in layer 5 of the cortex visual. *Right*. Confocal imaging of immunohistochemistry-
852 confirmed AAV GFAP-ChR2 (cyan) expression in astrocytes (S100β, magenta) in AnkG-GFP-
853 positive mice (green). **B.** *Left*. Photomicrography of the AIS (AnkG-GFP) in an L5PN filled with
854 Alexa 647 alongside an astrocyte expressing AAV GFAP-ChR2. **B.** *Middle*. Time course of
855 normalized spike number before and after optogenetic activation of astrocytes, with (purple)
856 or without (cyan) S100β antibody application, with representative traces above. *Right*.
857 Quantification of spike number changes in the last 10 minutes, with individual values for
858 each cell represented as cyan (optogenetic activation of astrocytes), purple (S100β antibody
859 followed by optogenetic activation of astrocytes). **C.** *Left*. Live image of an AnkG-GFP-
860 positive neuron filled with Alexa Fluor 647 before and after optogenetic activation of an
861 astrocyte expressing ChR2 (cyan). Black arrowheads indicate the start and end of the AIS.
862 *Right*. The optogenetic activation of astrocytes significantly elongates the length of the AIS.
863 **D.** *Left*. Live image of an AnkG-GFP-positive neuron fixed with Alexa Fluor 647 before and after
864 optogenetic activation of a ChR2-expressing astrocyte (cyan), with prior S100β antibody
865 application. Black arrowheads indicate the start and end of the AIS. *Right*. The application of
866 the S100β antibody, prior to optogenetic peri-AIS astrocyte activation, prevents changes in
867 AIS length. **E.** *Left*. Current-number of spike relationships for each condition (before and after
868 optogenetic activation of astrocytes). Optogenetic activation caused a leftward shift in the
869 mean curve. *Top*. Representative traces of individual current injections at different
870 amplitudes. Note the difference in the spike number with the same amplitude before and

after optogenetic activation of astrocytes. *Right*. Change in Rheobase in the recorded neuron during optogenetic peri-AIS astrocyte activation. **F.** *Left*. Current-number of spike relationships for each condition (before and after optogenetic astrocyte activation with prior S100β antibody application). *Top*. Representative traces of individual current injections at different amplitudes, with no changes observed. *Right*. No change in Rheobase in the recorded neuron during optogenetic peri-AIS astrocyte activation with prior S100β antibody application.

Figure 5. S100β rescues LTP-IE and AIS plasticity

A. *Left*. Experimental paradigm. Stimulation was performed by current injection into the whole-cell recorded neuron, with BAPTA-filled peri-AIS astrocyte inactivation and S100β protein applied 5 minutes before induction. *Middle*. Time course of normalized spike number before and after induction during peri-AIS astrocyte network inactivation (green) and following S100β application (orange), with representative traces shown above. *Right*. Quantification of spike number changes in the last 10 minutes, with individual values for each cell represented as green (astrocytes inactivated) and orange (astrocytes inactivated with prior S100β application) open circles. **B.** *Left*. Live image of an AnkG-GFP-positive neuron filled with Alexa Fluor 647 before and after induction during peri-AIS astrocyte (filled with Alexa Fluor 594) network inactivation, with prior S100β application. Black arrowheads indicate the start and end of the AIS. *Right*. S100β rescues the elongation of AIS length. **C.** *Left*. Current-number of spike relationships for each condition (before and after induction, during peri-AIS astrocyte network inactivation, with prior S100β application). Induction caused a leftward shift in the mean curve. *Right*. Representative traces of individual current injections at different amplitudes. Note the difference in the spike number with the same amplitude before and after induction, during peri-AIS astrocyte network inactivation, with prior S100β application. **D.** Change in Rheobase in the recorded neuron during peri-AIS astrocyte network inactivation with prior S100β application.

Supplementary Figure 1. AIS plasticity linked to LTP-IE emerges within minutes post-induction

Left. Time course of normalized spike count before and after induction (red), with representative traces shown above. Time course of normalized AIS length (green) measured every 5 minutes post-induction. Note the immediate change in excitability following induction and the increase in AIS length occurring 10–15 minutes later. *Right*. Individual AIS length measurements over time, with light gray representing individual cells and red indicating the average. Example images are shown at baseline (0 min, before) and 30 minutes (after) post-induction.

Supplementary Figure 2. Representation of the astrocyte optogenetic stimulation protocol

A. Photomicrograph of a patched astrocyte in whole-cell configuration, filled with Alexa Fluor 594 and expressing ChR2 (cyan) for the data presented in **B**. The ROI drawing represents the optogenetic stimulation area. **B.** *Top*. Membrane responses of the astrocyte in **A** to optogenetic stimulation (ROI), representing the complete stimulation protocol used in our experiments with VGlut2-AnkG-GFP mice injected with AAV GFAP-ChR2. *Bottom*. Expansion of a part of the stimulation protocol clearly showing how each scanning episode (2s) triggers a membrane depolarization.

Supplementary Figure 3. ATP/adenosine inhibition does not affect LTP-IE or AIS plasticity

A. *Left*. Experimental paradigm. Stimulation was performed by optogenetic activation of an astrocyte near the AIS of the recorded whole-cell neuron, after a 5-minute application of the ATP/adenosine antagonist Suramin. *Middle*. Time course of normalized spike number before and after induction during peri-AIS astrocyte optogenetic activation in the presence of Suramin (blue), with representative traces shown above. *Right*. Quantification of spike

926 number changes in the last 10 minutes, with individual values for each cell represented as
927 open blue circles (optogenetic activation of astrocytes in the presence of Suramin). **B.** *Left*.
928 Live image of an AnkG-GFP-positive neuron filled with Alexa Fluor 647 before and after
929 optogenetic activation of an astrocyte expressing ChR2 (cyan), with Suramin present. Black
930 arrowheads indicate the start and end of the AIS. *Right:* Suramin does not affect the
931 elongation of AIS length. **C.** *Left*. Current-number of spike relationships for each condition
932 (before and after optogenetic activation of astrocytes, under Suramin exposure).
933 Optogenetic activation caused a leftward shift in the mean curve. *Right*. Representative
934 traces of individual current injections at different amplitudes. Note the difference in the spike
935 number with the same amplitude before and after optogenetic activation of astrocytes, while
936 Suramin was applied. **D.** No change in Rheobase in the recorded neuron during optogenetic
937 activation of peri-AIS astrocyte network in the presence of Suramin.

938

939 **Supplementary Figure 4. BAPTA extracellular rescues LTP-IE and AIS plasticity**

940 **A.** *Left*. Experimental paradigm. Stimulation was performed by current injection into the
941 whole-cell recorded neuron, with BAPTA-filled peri-AIS astrocyte for inactivation of the
942 astrocytic syncytium and local extracellular application of BAPTA to mimic the Ca2+-
943 chelating action of S100β, 5 minutes before induction. *Middle*. Time course of normalized
944 spike number before and after induction during peri-AIS astrocyte network inactivation
945 (green) and following extracellular BAPTA application (brown), with representative traces
946 shown above. *Right*. Quantification of spike number changes in the last 10 minutes, with
947 individual values for each cell represented as green (astrocytes inactivated) and brown
948 (astrocytes inactivated with prior BAPTA extracellular application) open circles. **B.** Live image
949 of an AnkG-GFP-positive neuron filled with Alexa Fluor 647 before and after induction during
950 peri-AIS astrocyte (filled with Alexa Fluor 594) network inactivation, with prior extracellular
951 BAPTA application. Black arrowheads indicate the start and end of the AIS. *Right*. BAPTA
952 extracellular rescues the elongation of AIS length. **C.** *Left*. Current-number of spike
953 relationships for each condition (before and after induction, during peri-AIS astrocyte

network inactivation, with prior extracellular BAPTA application). Induction caused a leftward shift in the mean curve. *Right*. Representative traces of individual current injections at different amplitudes. Note the difference in the spike number with the same amplitude before and after induction, with prior BAPTA extracellular application. **D.** No change in Rheobase in the recorded neuron during peri-AIS astrocyte network inactivation with prior BAPTA extracellular application.

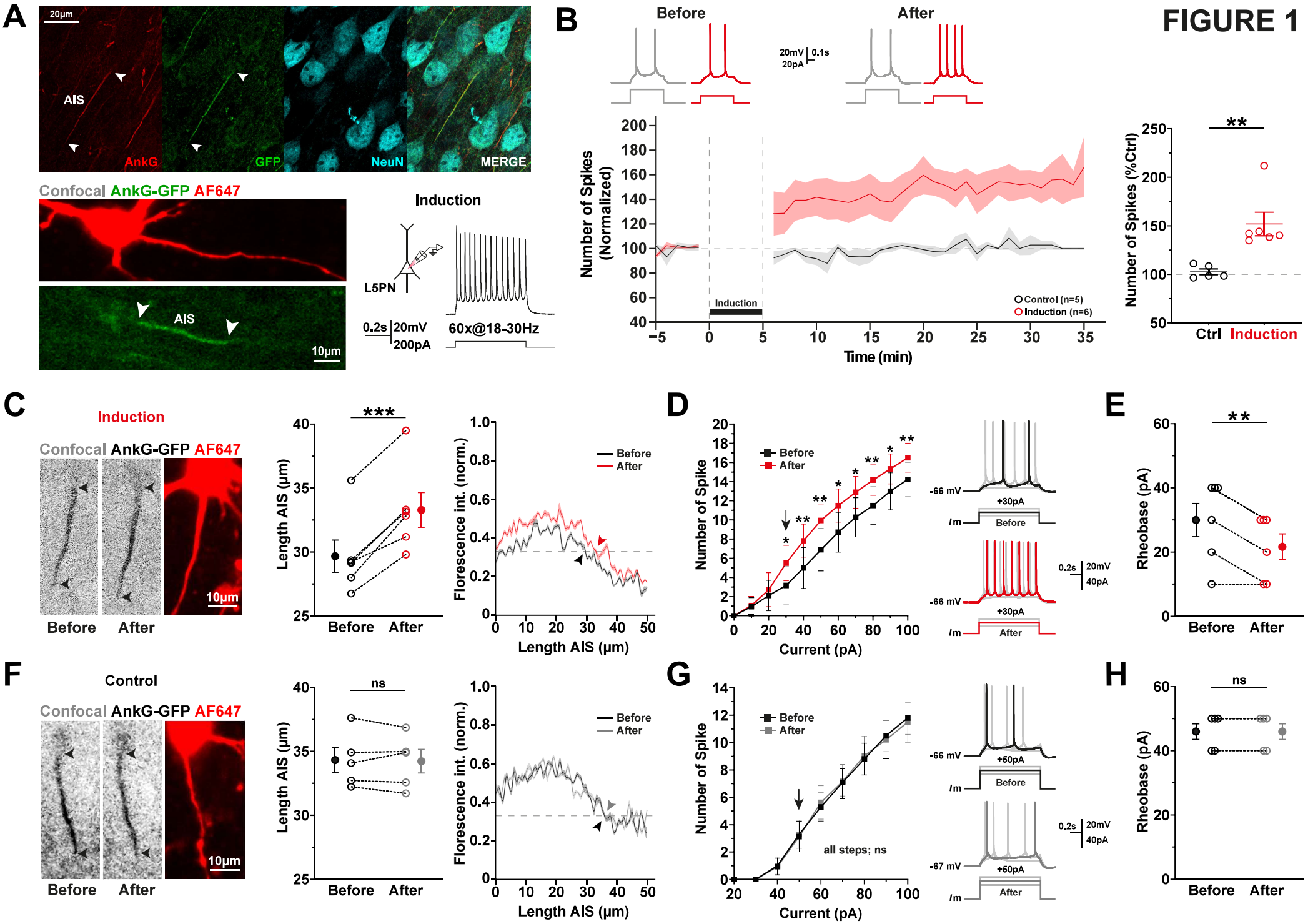
FIGURE 1
A
20µm
AIS
AnkG
GFP
NeuN
MERGE
Confocal AnkG-GFP AF647
AIS
10µm
Induction
L5PN
0.2s 20mV
200pA
60x@18-30Hz
B
Before
After
20mV 0.1s
20pA
Number of Spikes (Normalized)
Induction
Control (n=5)
Induction (n=6)
Time (min)
Number of Spikes (%Ctrl)
**
Ctrl
Induction
C
Induction
Confocal AnkG-GFP AF647
10µm
Before
After
***
Length AIS (µm)
Florescence int. (norm.)
Before
After
Length AIS (µm)
D
Number of Spike
Before
After
Current (pA)
-66 mV
+30pA
Im
Before
0.2s 20mV
40pA
-66 mV
+30pA
Im
After
E
**
Rheobase (pA)
Before
After
F
Control
Confocal AnkG-GFP AF647
10µm
Before
After
ns
Length AIS (µm)
Florescence int. (norm.)
Before
After
Length AIS (µm)
G
Number of Spike
Before
After
all steps; ns
Current (pA)
-66 mV
+50pA
Im
Before
0.2s 20mV
40pA
-67 mV
+50pA
Im
After
H
ns
Rheobase (pA)
Before
After

FIGURE 2

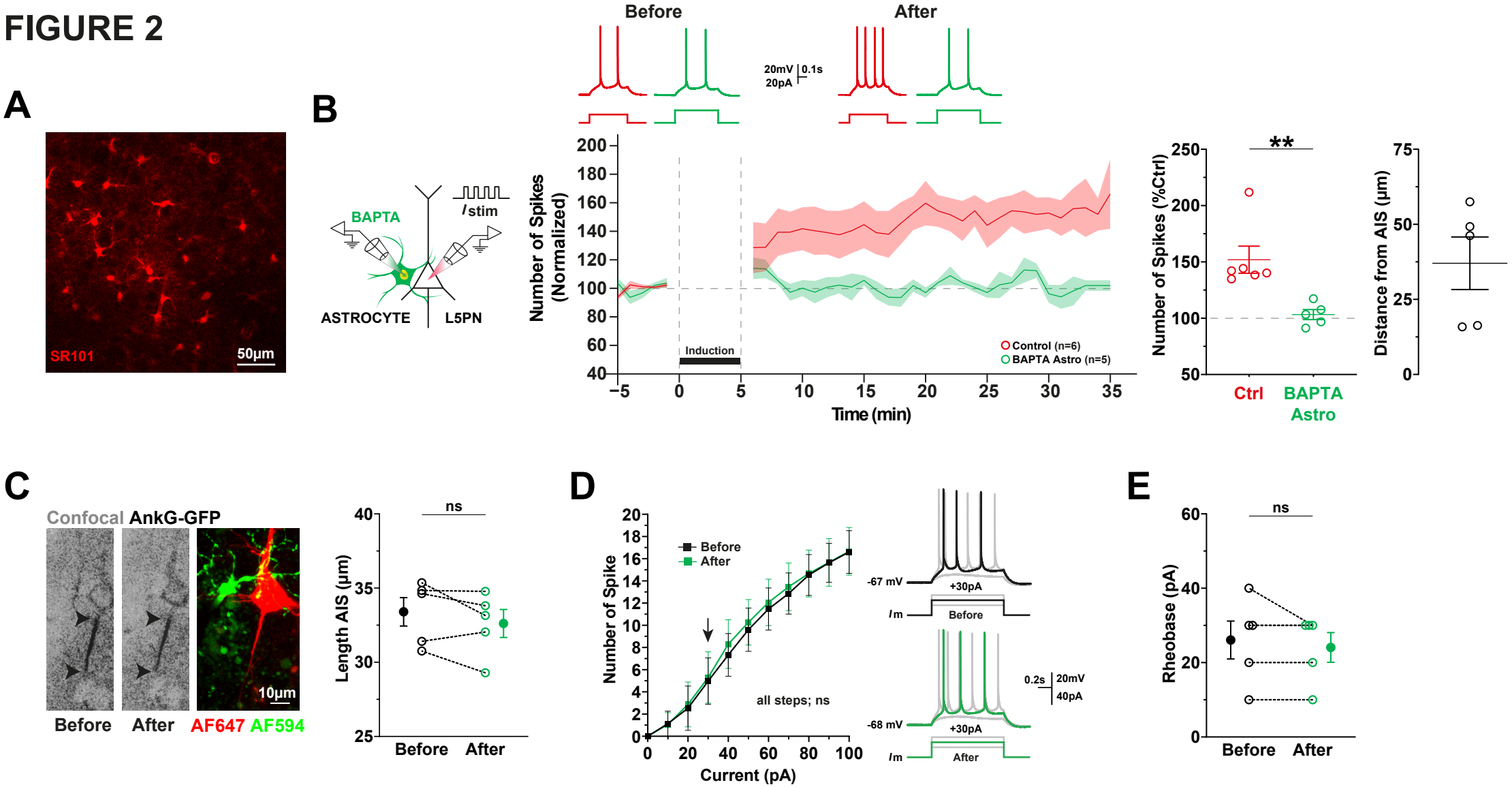
A
SR101
50µm
B
BAPTA
Istim
ASTROCYTE
L5PN
Before
After
20mV
0.1s
20pA
Number of Spikes (Normalized)
Induction
Control (n=6)
BAPTA Astro (n=5)
Time (min)
Number of Spikes (%Ctrl)
**
Ctrl
BAPTA Astro
Distance from AIS (µm)
C
Confocal AnkG-GFP
Before
After
AF647 AF594
10µm
Length AIS (µm)
ns
Before
After
D
Number of Spike
Before
After
all steps; ns
Current (pA)
-67 mV
+30pA
Im
Before
0.2s
20mV
40pA
-68 mV
+30pA
Im
After
E
Rheobase (pA)
ns
Before
After

FIGURE 3

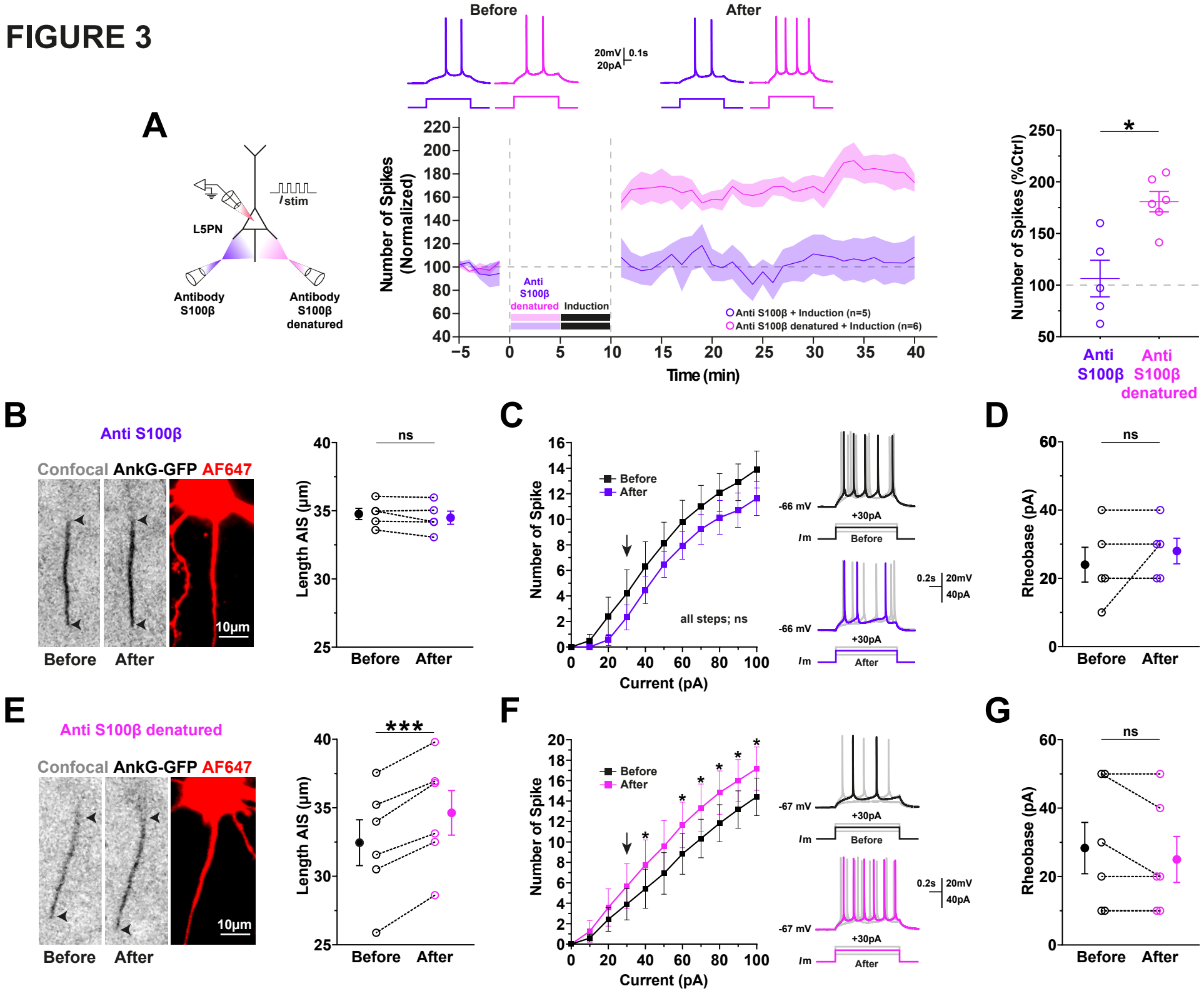
Before
After
20mV
0.1s
20pA
A
I stim
L5PN
Antibody S100β
Antibody S100β denatured
Number of Spikes (Normalized)
Anti S100β denatured
Induction
Anti S100β + Induction (n=5)
Anti S100β denatured + Induction (n=6)
Time (min)
Number of Spikes (%Ctrl)
Anti S100β
Anti S100β denatured
B
Anti S100β
Confocal AnkG-GFP AF647
10µm
Before After
Length AIS (µm)
ns
C
Number of Spike
Before
After
all steps; ns
Current (pA)
-66 mV
+30pA
Im
0.2s
20mV
40pA
D
Rheobase (pA)
E
Anti S100β denatured
***
F
-67 mV
G

FIGURE 4

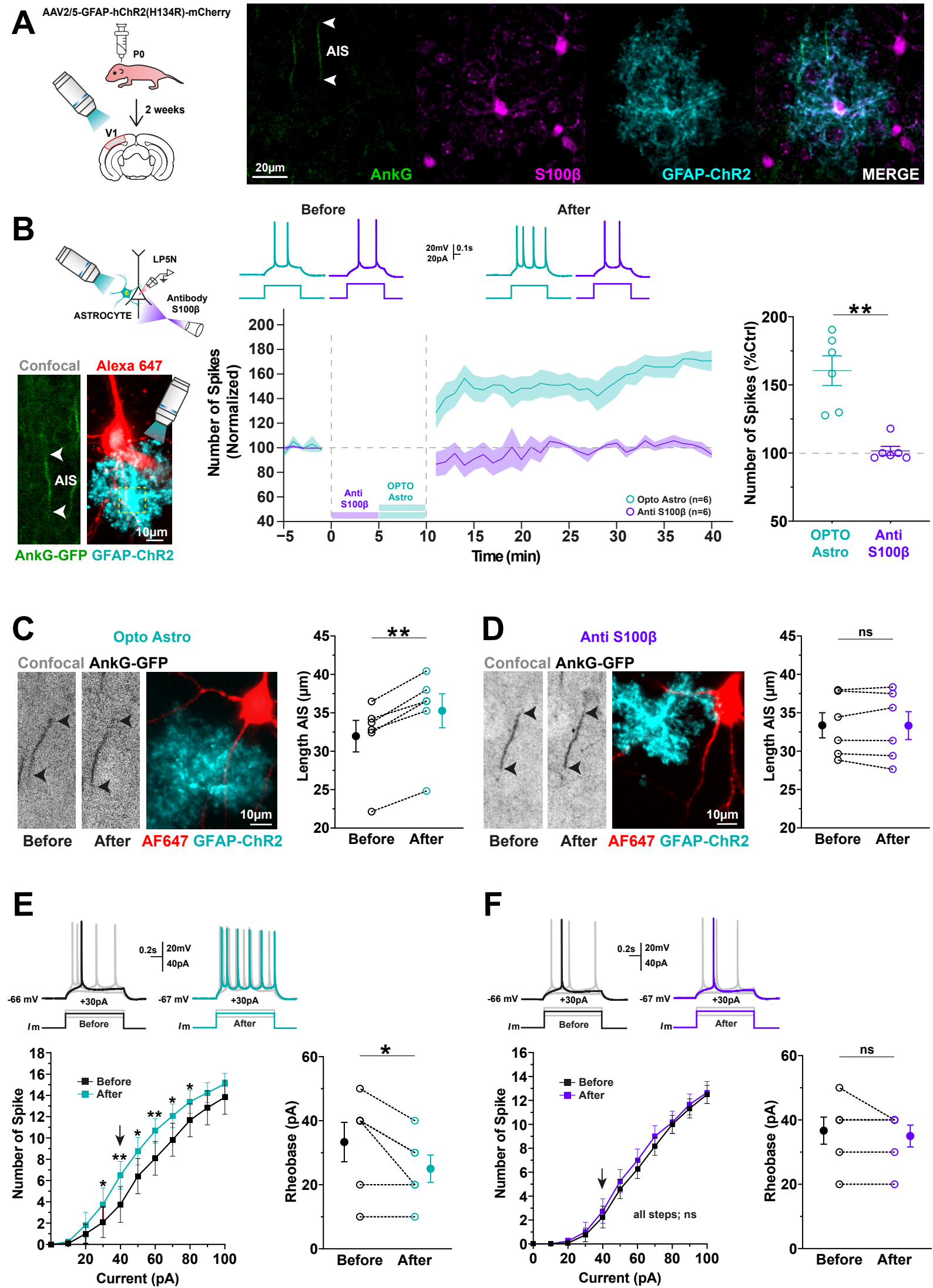
A
AAV2/5-GFAP-hChR2(H134R)-mCherry
P0
2 weeks
V1
AIS
20µm
AnkG
S100β
GFAP-ChR2
MERGE
B
LP5N
Antibody S100β
ASTROCYTE
Confocal
Alexa 647
AIS
10µm
AnkG-GFP GFAP-ChR2
Before
After
20mV
20pA
0.1s
Number of Spikes (Normalized)
Anti S100β
OPTO Astro
Opto Astro (n=6)
Anti S100β (n=6)
Time (min)
Number of Spikes (%Ctrl)
**
OPTO Astro
Anti S100β
C
Opto Astro
Confocal AnkG-GFP
10µm
Before After AF647 GFAP-ChR2
Length AIS (µm)
**
Before After
D
Anti S100β
Confocal AnkG-GFP
10µm
Before After AF647 GFAP-ChR2
Length AIS (µm)
ns
Before After
E
0.2s
20mV
40pA
-66 mV
+30pA
Im
Before
-67 mV
+30pA
Im
After
Number of Spike
Before
After
Current (pA)
Rheobase (pA)
*
Before After
F
0.2s
20mV
40pA
-66 mV
+30pA
Im
Before
-67 mV
+30pA
Im
After
Number of Spike
Before
After
all steps; ns
Current (pA)
Rheobase (pA)
ns
Before After

FIGURE 5

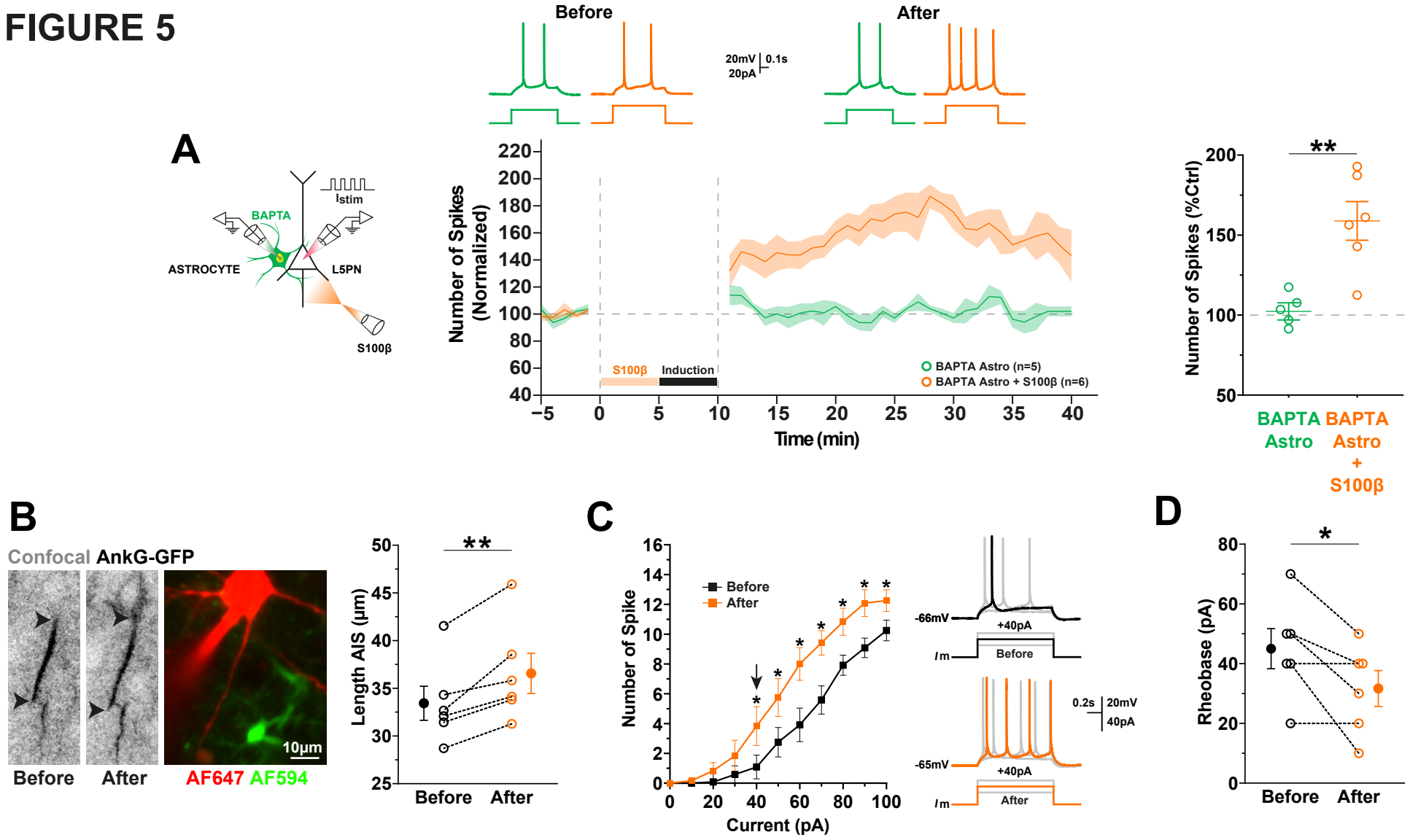
A
Before
After
20mV
0.1s
20pA
Istim
BAPTA
ASTROCYTE
L5PN
S100β
Number of Spikes (Normalized)
S100β
Induction
BAPTA Astro (n=5)
BAPTA Astro + S100β (n=6)
Time (min)
Number of Spikes (%Ctrl)
**
BAPTA Astro
BAPTA Astro + S100β
B
Confocal AnkG-GFP
Before
After
AF647 AF594
10µm
Length AIS (µm)
**
Before
After
C
Number of Spike
Before
After
Current (pA)
-66mV
+40pA
Im
Before
0.2s
20mV
40pA
-65mV
+40pA
Im
After
D
Rheobase (pA)
*
Before
After

Figure S1

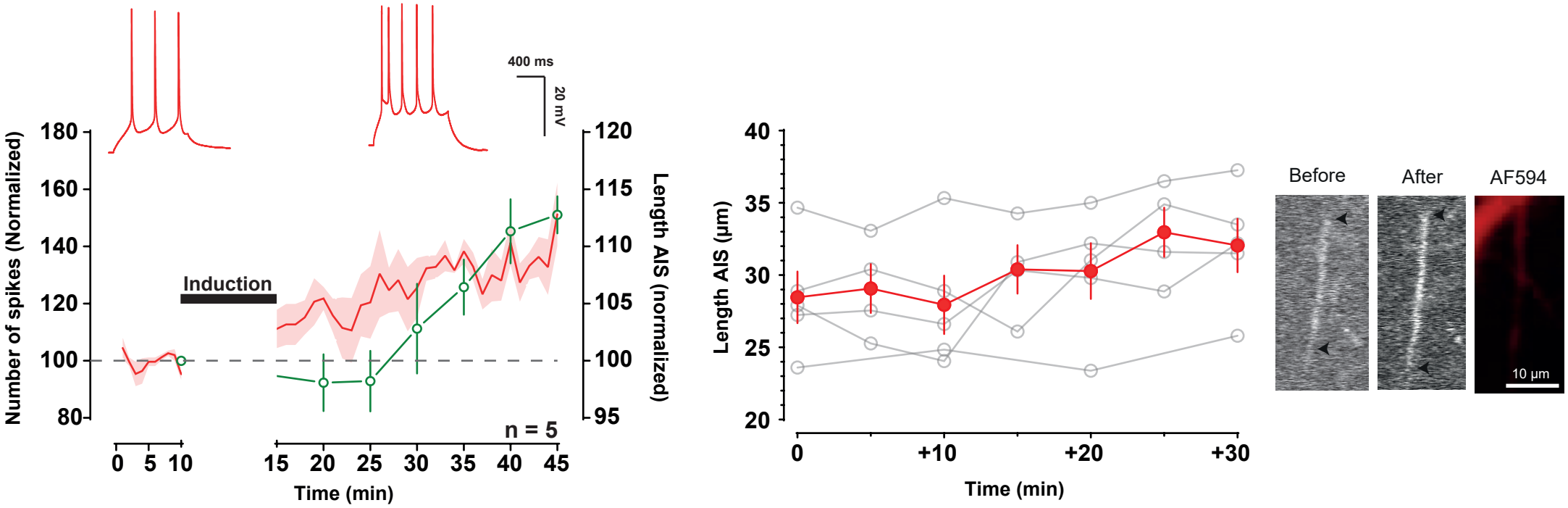
400 ms
20 mV
Number of spikes (Normalized)
180
160
140
120
100
80
Induction
Length AIS (normalized)
120
115
110
105
100
95
n = 5
0 5 10
15 20 25 30 35 40 45
Time (min)
Length AIS (µm)
40
35
30
25
20
0
+10
+20
+30
Time (min)
Before
After
AF594
10 µm

FIGURE S2

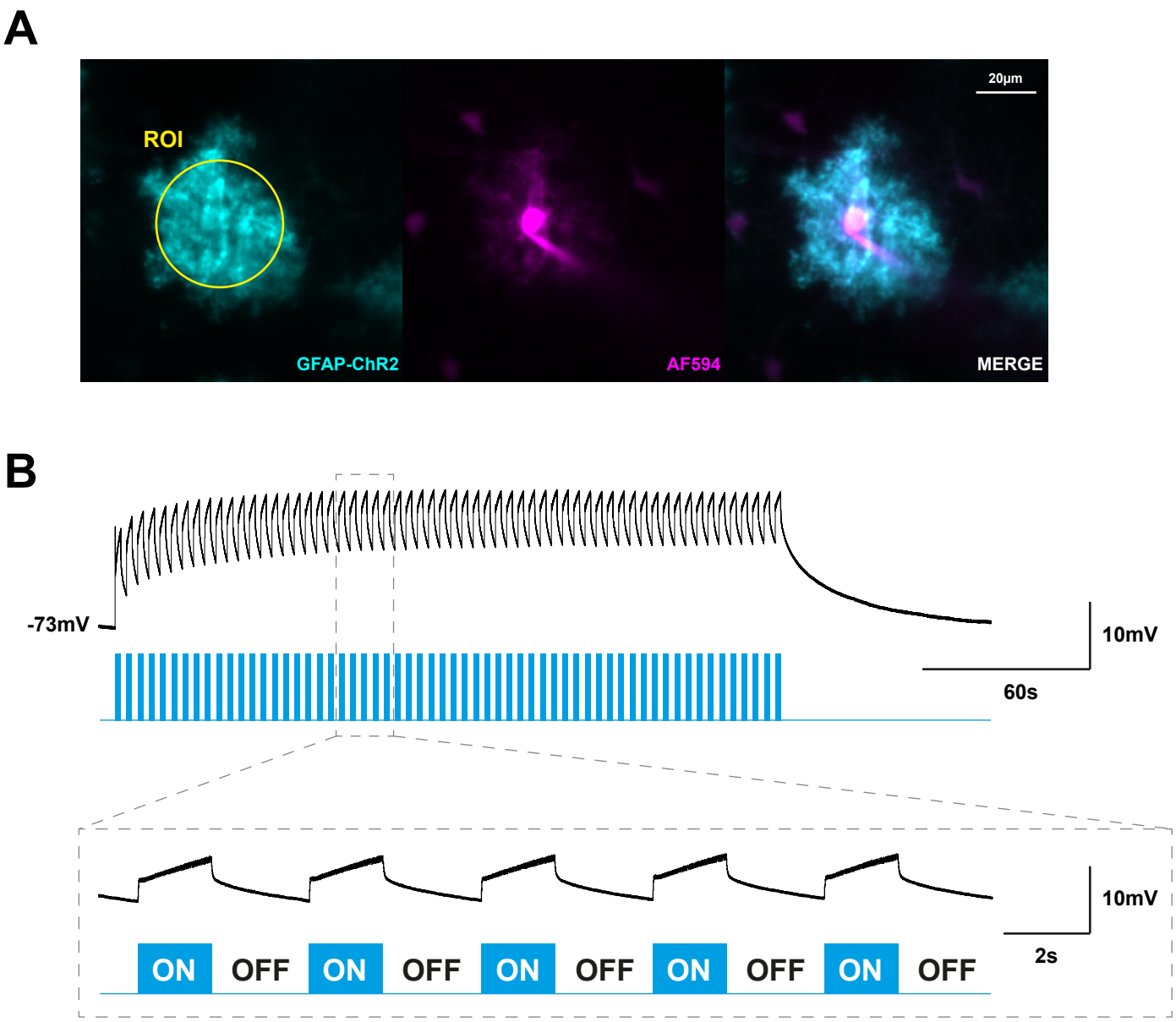
A
ROI
GFAP-ChR2
AF594
MERGE
20µm
B
-73mV
10mV
60s
10mV
2s
ON
OFF
ON
OFF
ON
OFF
ON
OFF
ON
OFF

FIGURE S3

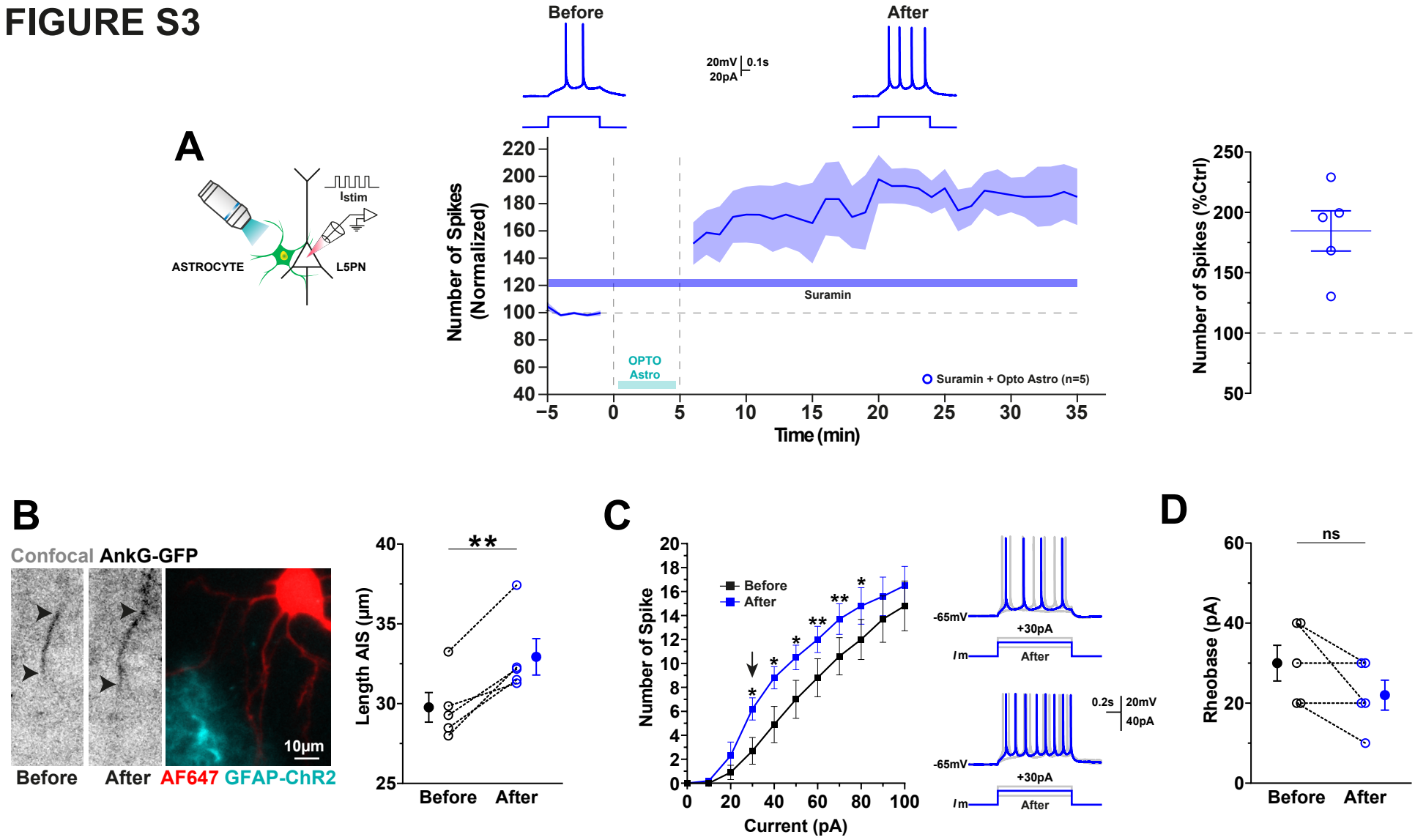
A
Istim
ASTROCYTE
L5PN
Before
After
20mV
0.1s
20pA
Number of Spikes (Normalized)
Suramin
OPTO Astro
Suramin + Opto Astro (n=5)
Time (min)
Number of Spikes (%Ctrl)
B
Confocal AnkG-GFP
10µm
Before
After
AF647 GFAP-ChR2
Length AIS (µm)
**
Before
After
C
Number of Spike
Before
After
Current (pA)
-65mV
+30pA
Im
After
0.2s
20mV
40pA
D
Rheobase (pA)
ns
Before
After

FIGURE S4

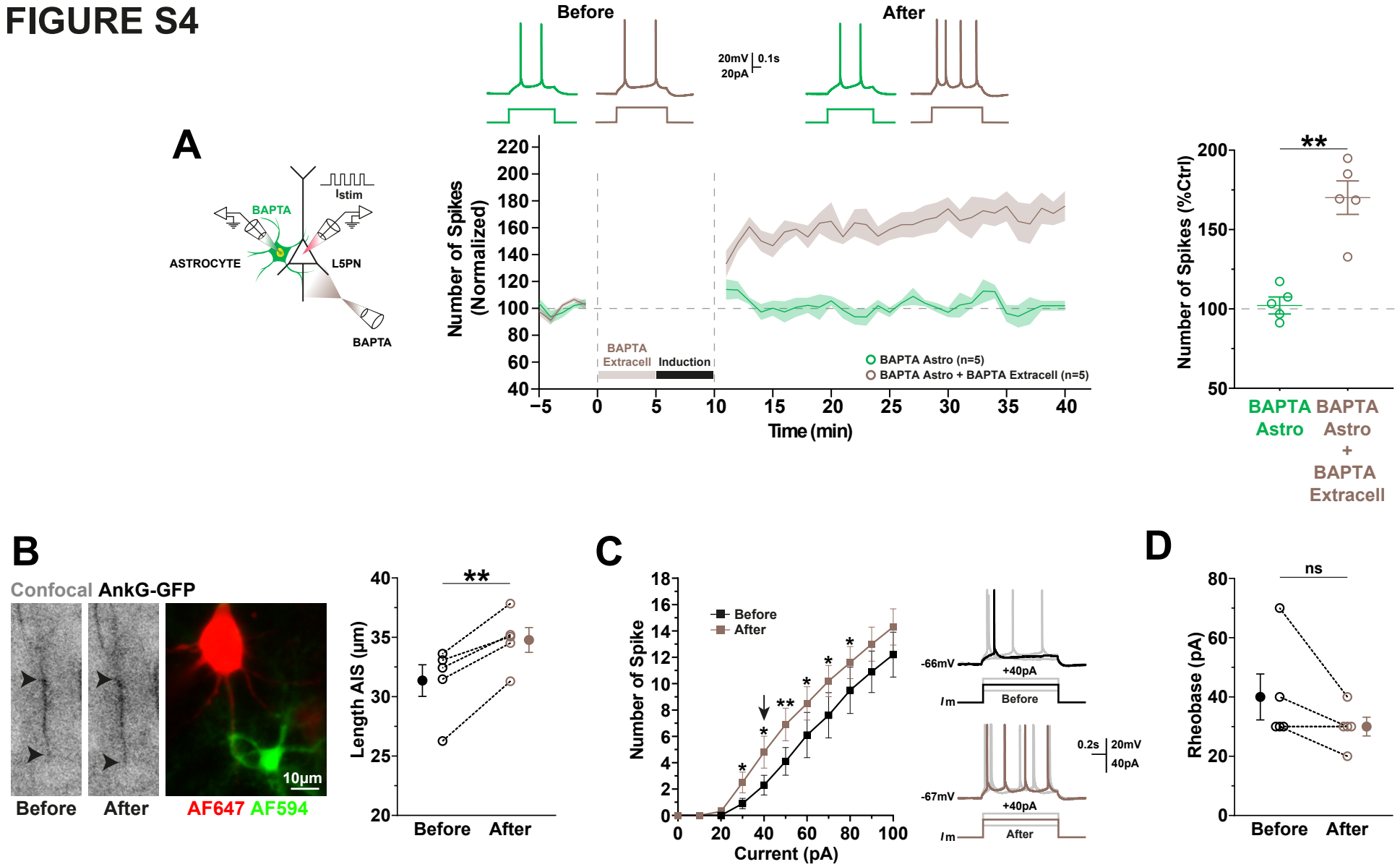
A
Before
After
20mV
0.1s
20pA
Istim
BAPTA
ASTROCYTE
L5PN
BAPTA
Number of Spikes (Normalized)
BAPTA Extracell
Induction
BAPTA Astro (n=5)
BAPTA Astro + BAPTA Extracell (n=5)
Time (min)
Number of Spikes (%Ctrl)
**
BAPTA Astro
BAPTA Astro + BAPTA Extracell
B
Confocal AnkG-GFP
Before
After
AF647 AF594
10µm
Length AIS (µm)
**
Before
After
C
Number of Spike
Before
After
Current (pA)
-66mV
+40pA
Im
Before
0.2s
20mV
40pA
-67mV
+40pA
Im
After
D
Rheobase (pA)
ns
Before
After